HSPI The Open Access Publisher

IJPRA ISSN 2766-2748 INTERNATIONAL JOURNAL OF PHYSICS RESEARCH AND APPLICATIONS

Research Article

Superconductivity Use for Redox Flow Batteries

Clifford M Krowne*

Chief Research Scientific Officer, Ashlawn Energy, LLC, 710 Resende Road, Bldg. 199, Webster, New York 14580, USA

Abstract

Here are presented ideas on moving power from the power grid to redox flow batteries, and the reverse. The thought is to provide the electrochemical stack unit with DC power from the power grid using high-temperature superconducting (SC) lines, which require the least maintenance, the lowest cost of materials, and the simplest solid-state chemistry employed to manufacture stable SC lines. The chemistry behind making the SC lines is provided in terms of discussing the electronic orbitals, the physics thought to underline the phenomenon, and ways to elevate the superconducting critical temperature T_C. The higher the T_C, the more likely SC technology is to be utilized.

More Information

***Corresponding author:** Clifford M Krowne, Materials Physics & Chemistry Section, Materials and Sensors Branches, Material Science & Technology Division, & Microwave Circuits & Electromagnetic Theory Sections, Microwave Technology & Electromagnetics Branches; Electronics Science & Technology Division, Naval Research Laboratory, 4555 Overlook Avenue, SW, Washington, DC 20375, USA,
Email: cliffordkrowne@outlook.com

Submitted: May 19, 2026
Accepted: May 30, 2026
Published: June 01, 2026

Citation: Krowne CM. Superconductivity Use for Redox Flow Batteries. Int J Phys Res Appl. 2026; 9(6): 145-161. Available from: https://dx.doi.org/10.29328/journal.ijpra.1001154

I. Introduction

In the past, our company has investigated many aspects of Redox Flow Batteries (RFBs) in order to advance understanding of the basic science and engineering, which would impact our efforts to manufacture Vanadium Redox Flow Batteries (VRFBs). This has included: quantum chemistry origin of the exponential unitless coefficients found in Taflove and Butler-Volmer equations allowing closed form nonlinear current-voltage analytical formulas [1]; Nernst equations showing dependence on overpotential in nonequilibrium [2,3]; governing equations required to describe the operation of a redox flow battery [4]; the role of fluid physics controlling the VRFB including ion crossover effects [5,6]; optical techniques involving spectroscopy to assess ion concentrations [7]; various measures of RFB performance such as Coulomb, voltage and energy efficiencies, and energy density [8]; State of Charge (SoC) contributions in bipolar plates and electrodes [9]; and charging requirements for starting up and maintaining cycling through time of the RFB [10]. An overview of using RFBs for residential, commercial, or medical facilities was provided too [11]. The last articles [10,11] hint at the best ways to go from the RFB system (stack, tanks, sensors, pumps, pipes, and monitoring computers) to the power grid.

The treatment in this paper aims to fill in a gap that has existed in the literature for many decades, which is whether or not to use AC or DC power grid lines and whether or not to use conventional aluminum/copper or other conventional metals, or to use superconducting lines, to feed into the RFB. The use of superconducting lines is known to allow the movement of power at a considerable reduction in losses (usually ohmic) compared to conventional metal lines. It would seem this would be the best alternative for feeding power to end users, such as those employing RFBs to store energy and providing power during power outages. The problem with that thought is that there is a considerable cost to providing the cooling systems required to lower the power line grid temperature T_{grid} below ambient temperature T_a enough that it is also less than the superconducting critical temperature T_C. That is,

$$T_{grid} < T_C < T_a$$

Well known is the advantage of using AC transmission along power lines because the losses are considerably less than those of DC transmission, especially for long distances. This truth does not hold for shorter grid movements, however. For shorter power distance transmission, the use of either AC or DC would be acceptable. For shorter distances, it might very well be viable economically to employ Superconducting (SC) lines. This would be helped enormously if the SC line materials had TCs higher than the readily available material $T_C's$, which are below 140 K, with commercially available materials with considerably lower $T_C's$. Note that room temperature is at about 300 K. There is another caveat, and that is the use of AC power transmission using SC lines induces eddy currents

with flow increasingly restricted to outer conducting SC surfaces as frequency increases. This problem does not occur for DC SC transmission. Figure 1 shows the two types of power transmission grids (AC and DC), and the required transformations from that grid's high voltage to the low voltage (but often high amperage of the redox flow battery stack) - at the bottom of each flow chart is found the VRFB. Figure 2 shows one of our stacks, which is contained in the last block diagram at the bottom of each flow chart. Figure 3 shows what a single-cell VRFB looks like internally regarding the electrochemistry, as well as the external equipment to run it.

The literature in the field of superconductivity is vast, and includes many efforts over the last nearly 40 years, earlier directed toward developing higher T_c materials beyond the first wave of those that shot up beyond the more traditional spherical band structures. Now the superconductive community knows about iron-based superconductors (pnictides, like Fe-doped LaOFeAs [12-14]), which can display a relatively high T_c. There are also more exotic superconductors, which can not advertise for high T_c applications. Rather, they are of interest ever since investigations into 2D materials showed that graphene layers of a single material have analogous properties to Dirac particles associated with studies in particle physics. What I am talking about here are graphene bilayers, which have the two layers slightly twisted with respect to their atomic lattice arrangement [15-17]. Of course, there are the more traditional low critical temperature materials, which are mostly pure metals like Hg or Pb, or alloys like niobium-titanium, germanium-niobium, or niobium nitride. Beyond the cuprate ceramic high T_c materials, there are others like magnesium diboride [18,19] with a T_c = 39 K. Under enormous pressure (90 GPa), H_2S has the highest T_c ever recorded at 203 K [20,21]. The Yttrium Barium Copper Oxide (YBCO) family of crystalline compounds has general formulas of $YBa_2Cu_3O_{7-x}$, $YBa_2Cu_4O_y$, $Y_2Ba_4Cu_7O_y$, with original T_c found to be 93 K [22]. This group of various stoichiometry oxides can be seen as part of the more general group labeled as ReBCO, with Re = rare earth element. Non-rare-earth high T_c superconductors were also found [23-28].

Sections that follow treat: quantum wave nature of the superconducting electrons (Section II); quantum wavefunction pairing overlap in the 3D lattice (Section III); orbital spatial characteristics (Section IV); relationship between energy interaction mechanisms and the critical superconducting temperature (Section V); trends of the superconducting materials about atomic or molecular mass, unit cell volume or atom counts (Section VI); a discussion (Section VII), and conclusions (Section VIII) (Figure 3).

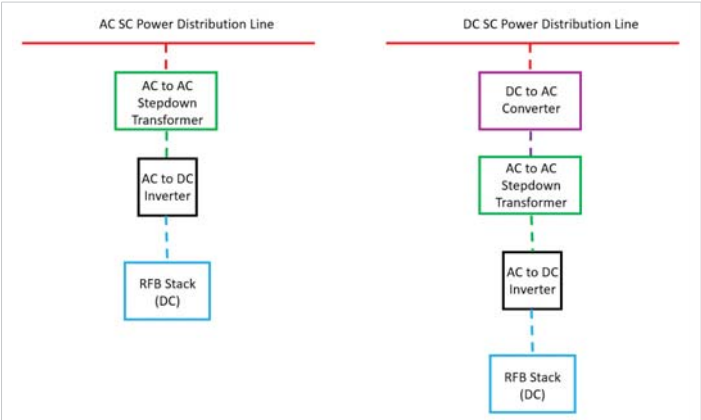

Figure 1: Power distribution grid types (AC SC line left-hand diagram; DC SC line right-hand diagram), with the required transformations needed to reach the redox flow battery stack.

Figure 2: Shown is an assembled Ashlawn 3-cell medium-sized vanadium redox flow battery stack, with electrolyte tanks and pumps for the negative and positive battery half-cells, with a computer for monitoring the stack (on the bench in the left-hand background). Controls for adjusting pump speeds are shown on the bench with the computer. Spill berm (black lattice insulating structure inserted into the yellow tub) for fluid containment is shown below the tanks, pumps, and stack. (Taken from [10].)

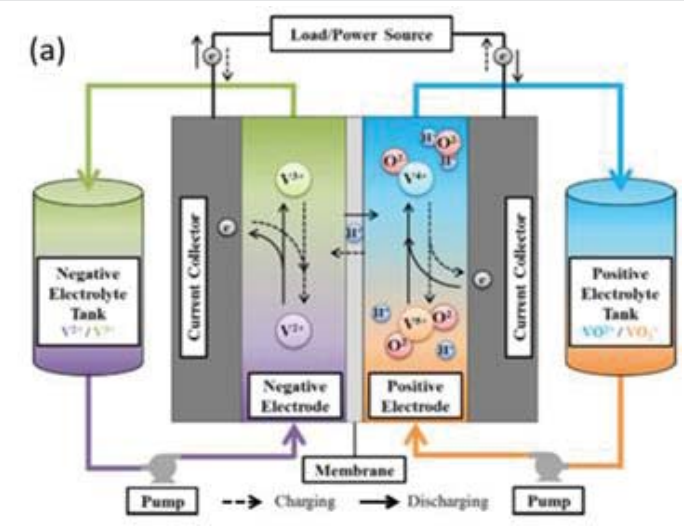

Figure 3: Shown is a single-cell VRFB, showing the internal stack chemistry and the external equipment to run that stack. This is a cross-sectional view. (Taken from [10].)

II. Quantum wave nature of the superconducting electrons

It is well understood that the electrons must pair up in twos to combine a spin-up electron with a spin-down electron, so that the combination has no net spin. When the electrons doing this share a common space, traveling together, one calls them Cooper pairs. Therefore, the basic unit of charge for superconductivity is $2e^-$, where e^- is the magnitude of the electron. An equivalent statement to saying the Cooper pair has no net spin is to say that their combined magnetic moment is zero. When such a pair presents itself to other electrons, there is no tendency to break up motion due to Faraday effects. However, there is still a net charge, albeit now $2e^-$, which presents itself to other electron pairs. This repulsive phenomenon will be dealt with later.

Often, one refers to superconductors as s-wave or d-wave, based on the orbital nature of the electron involved. Orbitals are determined by the various atomic constituents of the compound superconductor. Generally, one may also have *p*-wave or even f-wave superconductors. The direction of the wave may be forward or backward propagating, depending on the sign of the momentum vector **q**. For the s-wave electron, for its lowering (or destruction operator), one has

$$c_{\mathbf{k}_{s1},\sigma_1}(\omega_s,t) = c_{\mathbf{k}_{s1},\sigma_1}(\omega_s,0)e^{i(\mathbf{k}_{s1}\cdot\mathbf{r}-\omega_s t)} \tag{1}$$

Notice that the destruction operator is given in reciprocal momentum space. The only way for this electron to pair up with another electron in a common quantum space is for its momentum to be exactly opposite and equal in magnitude to the other electron's momentum. Thus,

$$c_{\mathbf{k}_{s2},\sigma_{s2}}(\omega_s,t) = c_{\mathbf{k}_{s2},\sigma_{s2}}(\omega_s,0)e^{i(\mathbf{k}_{s2}\cdot\mathbf{r}-\omega_s t)} \tag{2}$$

For all electron waves, the prefactor retains the fermion character of the operator, whereas the exponential factor stores the explicitly propagating wave nature for the quantized particles of motion.

Momentum and spin for the *s*-electrons must satisfy

$$\mathbf{k}_{s_1}+\mathbf{k}_{s_2}=0 \tag{3a}$$

$$\boldsymbol{\sigma}_{s_1}+\boldsymbol{\sigma}_{s_2}=0 \tag{3b}$$

We see from (3) that both momentum and spin are three-dimensional vectors.

Suppose that one considers *p*-wave superconductors. Then the quantum wave expressions become

$$c_{\mathbf{k}_{p1},\sigma_{p1}}(\omega_s,t) = c_{\mathbf{k}_{p1},\sigma_{p1}}(\omega_s,0)e^{i(\mathbf{k}_{p1}.\mathbf{r}-\omega_s t)} \tag{4}$$

$$c_{\mathbf{k}_2,\sigma_{p2}}(\omega_s,t) = c_{\mathbf{k}_{p2},\sigma_{p2}}(\omega_s,0)e^{i(\mathbf{k}_{p2}.\mathbf{r}-\omega_s t)} \tag{5}$$

Momentum and spin for the *p*-electrons must satisfy

$$\mathbf{k}_{p_1}+\mathbf{k}_{p_2}=0 \tag{6a}$$

$$\boldsymbol{\sigma}_{p_1}+\boldsymbol{\sigma}_{p_2}=0 \tag{6b}$$

What about the cuprate superconductors, with *d*-wave character? Then

$$c_{\mathbf{k}_{d1},\sigma_{d1}}(\omega_s,t) = c_{\mathbf{k}_{d1},\sigma_{d1}}(\omega_s,0)e^{i(\mathbf{k}_{d1}.\mathbf{r}-\omega_s t)} \tag{7}$$

$$c_{\mathbf{k}_{d2},\sigma_{d2}}(\omega_s,t) = c_{\mathbf{k}_{d2},\sigma_{d2}}(\omega_s,0)e^{i(\mathbf{k}_{d2}.\mathbf{r}-\omega_s t)} \tag{8}$$

Momentum and spin for the *d*-electrons must satisfy

$$\mathbf{k}_{d_1}+\mathbf{k}_{d_2}=0 \tag{9a}$$

$$\boldsymbol{\sigma}_{d_1}+\boldsymbol{\sigma}_{d_2}=0 \tag{9b}$$

But why look at the *d*-orbital as the last possible orbital to consider? At least the *f*-orbital could be in play to provide electrons. Let's add the f-orbital to our list and then obtain

$$c_{\mathbf{k}_{f1},\sigma_{f1}}(\omega_s,t) = c_{\mathbf{k}_{f1},\sigma_{f1}}(\omega_s,0)e^{i(\mathbf{k}_{f1}.\mathbf{r}-\omega_s t)} \tag{10}$$

$$c_{\mathbf{k}_{f2},\sigma_{f2}}(\omega_s,t) = c_{\mathbf{k}_{f2},\sigma_{f2}}(\omega_s,0)e^{i(\mathbf{k}_{f2}.\mathbf{r}-\omega_s t)} \tag{11}$$

Momentum and spin for the *f*-electrons must satisfy

$$\mathbf{k}_{f_1}+\mathbf{k}_{f_2}=0 \tag{12a}$$

$$\boldsymbol{\sigma}_{f_1}+\boldsymbol{\sigma}_{f_2}=0 \tag{12b}$$

Alright, so one has amassed a collection of possible orbital contributing electrons. Is this all to it? The answer is a resounding no! That is because, in principle, the two contributing electrons may arise from different orbitals. Available orbitals are the *s*-, *p*-, *d*-, and *f*-orbitals. As long as there is orbital electron quantum wavefunction overlap in 3D space, pairing could, in principle, occur. Thus, there is both self-orbital pairing, as well as inter-orbital pairing. How many combinations $C_{orbitals}$ are there for inter-orbital pairing? Consider there being two slots available. The first slot can take any one of 4 orbitals. The second slot has three remaining possibilities. However, the order in which the slots are filled is immaterial, as one is only counting pairs, not the order in which one made the pairs. The answer is

$$C_{orbitals}=\frac{4\cdot 3}{2!}=6 \tag{13}$$

So, is there a convenient way to express the association of any two orbital possibilities, regardless of whether they are intra-orbital or inter-orbital? The answer is yes, letting the two indices *i* and *j* be set to

$$i,j=s,p,d,f \tag{14}$$

Then the quantum wave expressions become

$$c_{\mathbf{k}_{i1},\sigma_{i1}}(\omega_i,t) = c_{\mathbf{k}_{i1},\sigma_{i1}}(\omega_i,0)e^{i(\mathbf{k}_{i1}\cdot\mathbf{r}-\omega_i t)} \tag{15}$$

$$c_{\mathbf{k}_{j2},\sigma_{j2}}(\omega_j,t) = c_{\mathbf{k}_{j2},\sigma_{j2}}(\omega_j,0)e^{i(\mathbf{k}_{j2}\cdot\mathbf{r}-\omega_j t)} \tag{16}$$

Momentum and spin for the *p*-electrons must satisfy

$$\mathbf{k}_{i_1}+\mathbf{k}_{j_2}=0 \tag{17a}$$

$$\sigma_{i_1} + \sigma_{j_2} = 0 \tag{17b}$$

Is one now done? The answer again is no. That is because, generally, one does not have a solid-state superconducting material that is made up of pure single atoms for high critical superconducting temperatures. Originally, superconductivity was found in pure metals, like mercury, tin, lead, thallium (Tl), niobium (Nb), aluminum (Al), and technetium (T_c). These metals, and others (see Table 1), are referred to as Type I superconductors.

When these Type I superconductors are cooled below their critical temperature, they expel all magnetic fields from their interior, a phenomenon known as the Meissner effect. They behave like diamagnets. Superconductivity stops once the applied magnetic field exceeds its critical magnetic field, and the material returns to a normal, resistive state. The critical field for a Type I superconductor is temperature-dependent and can be described by the equation:

$$H_C(T) = H_C(0)\left[1 - \left(\frac{T}{T_C}\right)^2\right] \tag{18}$$

Table 1: Elemental superconductors, with their critical superconducting temperatures T_c (K) and critical magnetic fields H_c (T). All are BCS-type SCs except Bi, Li, Rh, β-W, and Yb.

Element	T_c (K)	H_c (T)	Type (I or II)
Al	1.20	0.01	I
Bi	5.3×10^{-4}	5.2×10^{-6}	I
Cd	0.52	0.0028	I
Ga	1.083	0.0058	I
Hf	0.165		I
α-Hg	4.15	0.04	I
β-Hg	3.95	0.04	I
In	3.4	0.03	I
Ir	0.14	0.0016	I
α-La	4.9		I
β-La	6.3		I
Li	4.0×10^{-4}		I
Mo	0.92	0.0096	I
Nb	9.26	0.82	II
Os	0.65	0.007	I
Pa	1.4		I
Pb	7.19	0.08	I
Re	2.4	0.03	I
Rh	3.25×10^{-4}	4.9×10^{-6}	I
Ru	0.49	0.005	I
Sn	3.72	0.03	I
Ta	4.48	0.09	I
Tc	7.46 – 11.2	0.04	II
α-Th	1.37	0.013	I
Ti	0.39	0.01	I
Tl	2.39	0.02	I
α-U	0.68		I
β-U	1.8		I
V	5.03	1.0	II
α-W	0.015	0.00012	I
β-W	1 - 4		
Zn	0.855	0.005	I
Zr	0.55	0.014	I

Figure 4 demonstrates this quadratic expression for a Type I superconductor, and shows the contrasting case for a Type II superconductor, which possesses vortices of magnetic flux penetrating parts of the superconducting material when

$$H_{C1} < H_C(T) < H_{C2} \tag{19}$$

Type-I superconductors are pure metals with low critical temperatures, exhibiting perfect Meissner effect (complete field expulsion) and a sharp transition to normal state at a single critical field, making them "soft"; Type-II superconductors, often alloys or ceramics, have two critical fields, a "mixed state" (vortices of magnetic flux) between them, and can withstand much higher fields, making them "hard" and practical for strong electromagnets like MRI machines.

Let us think about these Type I superconductors, as to their orbital nature. Atomic orbitals have their electron wavefunctions overlapping in 3D real space, with contributions at any spatial location depending on the quantum probability or wavefunction to be at that location. Atoms in a perfect lattice of the elemental material consist of a repetitive pattern in 3D space. Orbital electron overlap for a pair depends on contributions from nearest neighbor atoms, next nearest neighbor atoms, and so on, moving through the 3D lattice. This does not preclude both electrons coming from the atom itself, if it possesses two or more electrons. Let's examine the highest T_C elemental superconductors from Table 1: T_c, Nb, and Pb. Their electron configurations are: T_c: [Kr] $4d^5\ 5s^2$; Nb: [Kr] $4d^4\ 5s^1$; Pb: [Xe] $4f^{14}\ 5d^{10}\ 6s^2\ 6p^2$. Therefore, Tc and Pb can get both paired electrons from the same atomic orbitals (respectively, the s- and p-orbitals) in the lattice, whereas Nb must find the second s-orbital electron from another atom in the lattice. Knowledge that the outermost electrons can act as Bloch electrons and cruise the entire lattice freely, guides us into understanding that this may not be much of a problem. But this still points up that even with elemental superconductors, accounting for the 3D lattice becomes relevant.

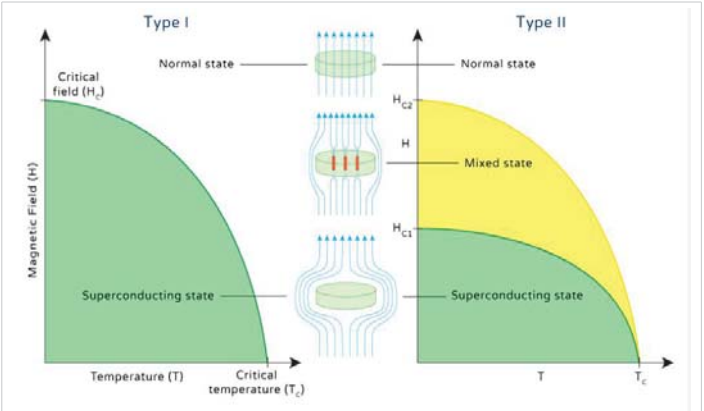

Figure 4: Type I (left diagram) and Type II (right diagram) superconductors, showing magnetic field *H vs. T*.

III. Examining the 3D lattice for quantum wavefunction pairing overlap

Pairing is promoted by various energy exchange mechanisms, which allow the Coulomb repulsion of the two electrons to be paired. Therefore, energy must be supplied to push the two electrons into enough proximity to be in mutual association. Call the mechanism energy $V_m^{en\,exch}\left(\mathbf{r}_1^{o_1,a_1},\mathbf{r}_2^{o_2,a_2}\right)$, which depends on the mechanism type m, electron positions, o_1, a_1, $\mathbf{r}_1$ and o_2, a_2, $\mathbf{r}_2$. This interaction energy must be weighted by each electron's probability to be present in real space to allow the energy exchange to allow pairing. Electron 1's wavefunction is $\psi_1^{o_1,a_1}(\mathbf{r}_1^{o_1,a_1})$, whereas the second electron's wavefunction is $\psi_2^{o_2,a_2}(\mathbf{r}_2{}^{o_2,a_2})$. Orbital type is o_1 for the first electron, and o_2 for the second electron. Electron orbitals arise from different lattice atoms, of type a_1 for the first electron and a_2 for the second electron. The total electron wavefunction for the first electron arises from summing over the entire lattice, perhaps in a tight-binding approximation. Therefore,

$$\psi_1^T(\mathbf{r}_1)=\sum_{o_1}\sum_{a_1}\psi_1^{o_1,a_1}\left(\mathbf{r}_1^{o_1,a_1}\right) \tag{19}$$

Similarly, for the second electron of the pair,

$$\psi_2^T(\mathbf{r}_2)=\sum_{o_2}\sum_{a_2}\psi_2^{o_2,a_2}\left(\mathbf{r}_2^{o_2,a_2}\right) \tag{20}$$

Equations (19) and (20) are atom-specific orbital electron wave functions. They also contain electron spin information to be complete. This could be put in explicitly, or one can append a spin index, σ, to each wavefunction. The result of the latter is

$$\psi_{1,\sigma_1}^T(\mathbf{r}_1)=\sum_{o_1}\sum_{a_1}\psi_{1,\sigma_1}^{o_1,a_1}\left(\mathbf{r}_1^{o_1,a_1}\right) \tag{21}$$

$$\psi_{2,\sigma_2}^T(\mathbf{r}_2)=\sum_{o_2}\sum_{a_2}\psi_{2,\sigma_2}^{o_2,a_2}\left(\mathbf{r}_2^{o_2,a_2}\right) \tag{22}$$

One may readily employ the Bloch theorem (use of this theorem for finding the tight binding electronic structure of 2D hexagonal materials is seen in Krowne, Chapter 3 of Advances in Imaging and Electron Physics, Vol. 210, 2019 [29]) to find the resulting wavefunctions at the various atomic locations, being careful to keep track of each atom location in the lattice, where atom, has a_1.

$$\mathbf{r}_1^{o_1,a_1}=R_{1;0}-R_{atom;i}^{lattice}\;;R_{1;0}=\mathbf{r}_1^{origin} \tag{23}$$

At this point in the discussion, one is at the point of being able to calculate the matrix element of the interaction, the interaction Hamiltonian of the electron pair system. One finds for the m[th] mechanism,

$$H_{interaction,m}^{Cooper\ pair}=\iiint_{r1}\iiint_{r2}\left[\psi_{1,\sigma_1}^T(\mathbf{r}_1)\right]^{\dagger}V_m^{en\,exch}\left(\mathbf{r}_1^{o_1,a_1},\mathbf{r}_2^{o_2,a_2}\right)\psi_{2,\sigma_2}^T(\mathbf{r}_2)d^3\mathbf{r}_1d^3\mathbf{r}_2 \tag{23}$$

Considering all mechanisms,

$$H_{interaction,T}^{Cooper\ pair}=\sum_m H_{interaction,m}^{Cooper\ pair} \tag{24}$$

One can point out here that examination of the properties of 2D materials has been of great interest recently [30-33], although here examination of more 3D-like SC's is treated, but one should be aware that 3D or lower-dimensional 2D or thin film SCs are relevant [34-37]. Even 1D materials are of interest, like nanowires, but they are less relevant for SC [38-40].

IV. Consideration of the orbital spatial characteristics

It would be useful at this point to examine the various orbital spatial distributions and determine which of them are most favorable, if any, for Cooper pair associations. Figure 5 shows the distributions in angular space.

In an atom, the principal quantum number n describes the energy of an electron and is associated with many orbitals. And n = positive integer. The orbitals associated with a particular n are said to reside within the nth shell. An azimuthal quantum number l characterizes the orbital angular momentum of an electron, is an integer, and $l \geq 0$. The range of l is $0 \leq l \leq n-1$. The last quantum number required to describe electron motion around the nucleus is the magnetic quantum number m_l. It represents the projection of the orbital angular momentum along a chosen axis, and determines the magnitude of the circulating electron current about that axis, giving the magnetic moment of that electron. Its range

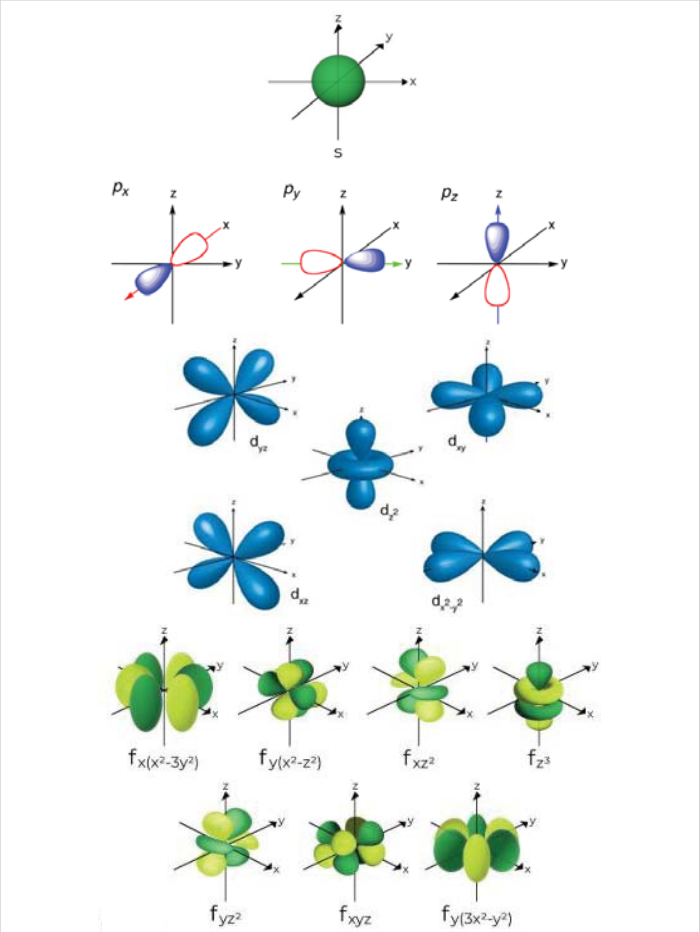

Figure 5: Graphical 3D sketches of the s, p, d, and f electron orbitals for the atomic nucleus, showing the angular distributions.

of values is $-l \le m_l \le l$. For a given n and value l, the range of m_l gives those subshell orbitals.

As is apparent, the larger n is, the more orbitals are found within each l subshell. And this is why one must enter the lanthanum group with n = 4, to get f orbitals.

The wave function describing the above considerations is the well-known form [41]

$$\psi_{n,l,m}(r,\theta,\phi) = R_{nl}(r) Y_l^m(\theta,\phi) \quad (25)$$

Here $R_{nl}(r)$ is the radial part of the wavefunction and $Y_l^m(\theta,\phi)$ is the complex spherical harmonic part of the wavefunction.

The quantum mechanical representation of the complex spherical harmonic is

$$Y_l^m(\theta,\phi) = (-1)^m \sqrt{\frac{(2l+1)}{4\pi}\frac{(l-1)!}{(l+1)!}} P_l^m(cos\theta) e^{im\phi} \quad (26)$$

Here P_l^m are the associated Legendre polynomials. Radial $R_{nl}(r)$ quantum mechanical part of the wavefunction satisfies the Schrodinger differential equation

$$r^2 \frac{d^2 R_{nl}(r)}{dr^2} + 2r \frac{dR_{nl}(r)}{dr} + \left[\frac{2m_e E_n}{\hbar^2 r^2}\right] - l(l+1) R_{nl}(r) = 0 \quad (27)$$

The Cartesian polynomial representation shown in Table 2 arose as a desirable way to display the complex wavefunction in a real 3D form, by noting that superpositions of wavefunctions can be valid quantum mechanical solutions of the atomic orbital equation. This is while realizing that such superpositions, based upon complex exponential expansions in sinusoidal functions, generate real numbers.

$$e^{im\phi} + e^{-im\phi} = \left[cos(m\phi) + isin(m\phi)\right] + \left[cos(m\phi) - isin(m\phi)\right] = 2cos(m\phi) \quad (28)$$

Inspection of the spherical s electron orbital shows that it is omnidirectional, allowing equal interaction with a quantized wave. Thus, s orbitals are extremely desirable if they are available in the superconductor material being considered. And this is why superconductivity was first discovered and even understood with the first detailed theoretical model, the Bardeen-Cooper-Schrieffer (BCS) model, for both pure elemental metals and compounds. This is also why exposed s orbitals should be very desirable for any higher temperature superconductors. Embedded s orbitals may be shielded by more exterior orbitals, and this would likely reduce their effectiveness in interacting with the propagating nonlocal quantum waves.

Table 2: Cells showing subshells, allowable for a particular shell, angular momentum quantum number (n, l) set, up to l = 4, n = 5.

	l = 0 (s)	l = 1 (p)	l = 2 (d)	l = 3 (f)	l = 4 (g)
n=1	m_l = 0				
n=2	0	-1, 0, 1			
n=3	0	-1, 0, 1	-2, -1, 0, 1, 2		
n=4	0	-1, 0, 1	-2, -1, 0, 1, 2	-3, -2, -1, 0, 1, 2, 3	
n=5	0	-1, 0, 1	-2, -1, 0, 1, 2	-3, -2, -1, 0, 1, 2, 3	-4, -3, -2, -1, 0, 1, 2, 3,4

The next orbital group is the p electron orbitals. They have no omnidirectional character. Instead, they have coordinated directional preferences. So these are much less desirable for interaction capability with the propagating quantized waves, as they intersect with a much smaller solid angle 3D cross-section. However, as noted by various workers, they may be instrumental in shuttling charges from one part of a unit cell to another, particularly important in many of the complicated cuprate compound superconductors.

Cuprate superconductors have the advantage of d electron orbitals. Their d_{xy}, d_{xz}, d_{yz} orbitals have twice as many lobes as p orbitals, so they will have a much larger solid angle 3D cross-section with which to intersect with the propagating quantized waves. Furthermore, of the other two d orbitals, the $d_{x^2-y^2}$ adds again for lobes in the xy-plane (with excursions into the z-direction). Finally, the last d orbital, the, has two lobes in the z-direction (like one of the p orbitals), but also an xy-plane omnidirectional lobe which should enhance xy-plane interactions with the propagating quantized waves. One concludes copper is an ideal d orbital atom for superconductivity. Recall that copper has the orbital structure [Ar] $3d^{10}$ $4s^1$, which is a remarkable situation. This is because copper atoms have a full d subshell filling, meaning that the maximum number of electrons consistent with the Pauli exclusion principle exists. There are ten times the number of electrons in copper's d subshell with which to interact with the propagating quantized waves.

So, one wonders if there are possible f orbital electrons available in great numbers to interact with the propagating quantized waves. One does not get to this point in electron occupancy for f orbital atoms until one reaches dysprosium with electron orbital structure [Xe] $4f^{10}$ $6s^2$. The f orbitals have 4, 6, or 8 lobes, with one omnidirectional in the xy-plane (the d_{z^3} orbital, which has two lobes and two rings, nominally 4 lobes). Six lobed f orbitals are the $f_{x\left(x^2-3y^2\right)}$, $f_{y\left(3x^2-y^2\right)}$, f_{xz^2}, f_{yz^2}. Eight lobed f orbitals are the $f_{y\left(x^2-z^2\right)}$ and the f_{xyz}. Therefore, one sees that the f orbitals, with their rich lobe structure, provide ample opportunity for a significant solid angle 3D cross-section, with the The eight lobed, $f_{x\left(x^2-3y^2\right)}$, $f_{y\left(3x^2-y^2\right)}$ orbitals are particularly effective interaction with the propagating quantized waves. For good interaction in a plane, consider the six lobed f orbitals $f_{x\left(x^2-3y^2\right)}$, $f_{y\left(3x^2-y^2\right)}$, f_{xz^2}, f_{yz^2}, which for the first two handle the xy-plane, whereas the other two handle the xz-plane and yz-plane. Finally, the d_{z^3} orbital has a mediocre quasi-omnidirectional character.

V. Relating energy exchanging mechanisms to critical temperature

There is a logarithmic expression that relates the critical temperature T_C to the sum of the energy interaction mechanisms involving the electron pairs, with each particular mechanism. It is a sophisticated expression based upon second

quantization arguments and renormalization techniques [42,43], and may be stated as

$$H_{interaction,T}^{Cooper\ pair}=\frac{2}{V_{vol}d\left(\epsilon_F\right)}\frac{1}{\left[\ln C_{scaling}-\ln T_C\right]} \tag{29}$$

The way to interpret this expression is that as one adds more energy exchange mechanisms, enlarging the left-hand side of (29), the logarithm of the critical temperature In T_C must rise, catching up to the other logarithm in the denominator. The units of the density of states at the Fermi energy, d, are in $1/ergs\cdot cc$, whereas the unit cell crystal lattice volume is in cc, making the product $1/ergs$. Since $C_{scaling}$ is in units of Kelvin, the logarithmic difference found in (29) is unitless. Equation (29) may be solved for this logarithmic difference,

$$\left[\ln C_{scaling}-\ln T_C\right]=\frac{2}{V_{vol}d\left(\epsilon_F\right)}\frac{1}{H_{interaction,T}^{Cooper\ pair}} \tag{29}$$

As T_C rises, the left-hand-side difference approaches zero, which is the same as saying

$$\lim_{T_C\to C_{scaling}} H_{interaction,T}^{Cooper\ pair}\to\infty \tag{30}$$

Therefore, one must conclude that $C_{scaling}$ forms some unattainable upper limit, because there is no physical way the sum of all the energy exchange mechanisms transferring energy between the electron pairs and each mechanism, summed, can be infinite. Thus, one may state the following for the maximum critical superconducting temperature,

$$T_C^{min}<T_C^{max}<C_{scaling} \tag{31}$$

Here $C_{scaling}$ can be written, if one assumes only one mechanism is responsible for the majority of energy transfer, as

$$C_{scaling}=\frac{\langle\alpha_m\rangle}{\pi}\frac{\langle\hbar\omega_m\rangle}{k_B} \tag{32}$$

Here, $\hbar$ is the reduced Planck's constant, and k_B is Boltzmann's constant, given respectively, by $1.054571817\times10^{-27}\,erg\cdot sec$ and $1.3806\times10^{-16}\,erg/K$. Therefore, the second ratio yields temperature. The first ratio is unitless.

Averages over the mechanism types are given by

$$\langle\alpha_m\rangle=\sum_m\frac{\alpha_m}{N_m} \tag{33a}$$

$$\langle\omega_m\rangle=\sum_m\frac{\omega_m}{N_m} \tag{33b}$$

Here ω_m are the characteristic mechanism energies, α_m their weights, and N_m the total number of mechanisms.

Consider the upper inequality in (31).

$$T_C^{max}<C_{scaling} \tag{34}$$

Convert this to an equality, and substitute in (32).

$$T_C^{max}=\frac{\langle\alpha_m\rangle}{\pi}\frac{\langle\hbar\omega_m\rangle}{k_B} \tag{35}$$

Once one decides on a desirable maximum critical superconducting temperature, the averaged mechanism characteristic frequency of the interactions is pinned down. That is,

$$\langle\omega_m\rangle=T_C^{max}\frac{\pi}{\langle\alpha_m\rangle}\frac{k_B}{\hbar} \tag{36}$$

Since each alpha factor α_m is on the order of unity,

$$\langle\alpha_m\rangle\sim1 \tag{37}$$

Also, the Boltzmann to reduced Planck constant ratio is,

$$\frac{k_B}{\hbar}=1.31\times10^{11}K^{-1}\cdot s^{-1} \tag{38}$$

To convert this expression into something recognizable, it is useful to relate eV to ergs. The conversion is $1eV=1.60218\times10^{-12}\,erg$. By (36),

$$\hbar\langle\omega_m\rangle=k_BT_C^{max}\frac{\pi}{\langle\alpha_m\rangle} \tag{39}$$

Using the conversion,

$$\hbar\langle\omega_m\rangle=0.8617\times10^{-4}T_C^{max}\frac{\pi}{\langle\alpha_m\rangle}eV \tag{40}$$

If one sets T_C^{max} to be room temperature, namely about 300 K, useing (37), then (40) yields

$$\hbar\langle\omega_m\rangle\approx0.08eV \tag{41}$$

However, (35) and (41) are not correct for many mechanisms, some contributing equally to the energy exchange. Energy exchange is an additive, not an averaged effect. Therefore, the correct expression is

$$C_{scaling}=\frac{\langle\alpha_m\rangle}{\pi}\frac{\Sigma_m\hbar\omega_m}{k_B} \tag{42}$$

Giving

$$T_C^{max}=\frac{\langle\alpha_m\rangle}{\pi}\frac{\Sigma_m\hbar\omega_m}{k_B} \tag{43}$$

Equation (43) demonstrates a fundamental property of the energy exchange mechanisms. That they are additive in the renormalization second quantization model, when contributing to the critical superconducting temperature. The more viable mechanisms that can be realized when making a compound superconducting lattice, the higher the possible T_C^{max}. Thus, one should strive for compound superconducting materials which have as many possible mechanisms as obtainable.

VI. Atomic/molecular mass, unit cell volume, atom count trends

It was long ago recognized that for single-atom, elemental superconductors, the critical temperature seemed to be related to the atomic mass. Let us take a look again at this trend. First note that the isotope effect was confirmed, which showed that if there were several isotopes, the heavier isotopes had higher critical temperatures. This was one of the original confirmations of the Bardeen-Cooper- Shrieffer (BCS) theory of superconductivity. Take eleven elements from Table 1,

Table 3: Cartesian polynomial names for atomic orbitals.

	$\psi_{m=-3} + \psi_{m=3}$	$\psi_{m=-2} + \psi_{m=2}$	$\psi_{m=-1} + \psi_{m=1}$	$\psi_{m=0}$	$\psi_{m=-1} - \psi_{m=1}$	$\psi_{m=-2} - \psi_{m=2}$	$\psi_{m=-3} - \psi_{m=3}$
$l = 0$				s			
$l = 1$			p_y	p_z	p_x		
$l = 2$		d_{x2-y2}	d_{yz}	d_{z2}	d_{xz}	d_{xy}	
$l = 3$	$f_{y(3x2-y2)}$	$f_{y(x2-z2)}$	f_{yz2}	f_{z3}	f_{xz2}	f_{xyz}	$f_{x(x2-3y2)}$

plotting each of their T_C's against atomic weight AW, as shown in Figure 6. The purple line shows the overall trend, which supports the idea that larger AW leads to a higher T_c. But this is only an approximate trend, as there are two outliers, vanadium V and hafnium Hf.

One can also calculate the unit cell volumes of the elemental superconductors plotted in Figure 6. Element lattice constants and their crystal structures are given in Table 4. The volume results are provided in Table 5, after enlisting the following formulas for the unit cell volumes:

$$V^{unit\ cell}_{cubic,\ face-centered} = a^3 \tag{44a}$$

$$V^{unit\ cell}_{cubic,body-centered} = a^3 \tag{44b}$$

$$V^{unit\ cell}_{tetragonal,\ face-centered} = a^2 c \tag{44c}$$

$$V^{unit\ cell}_{orthorhombic,body-centered} = abc \tag{44d}$$

$$V^{unit\ cell}_{hexagonal,close-packed} = \frac{3\sqrt{3}a^2 c}{2} \tag{44e}$$

$$V^{unit\ cell}_{rhombohedral} = a^3\left(1-\cos(\alpha)\right)\sqrt{1+2\cos(\alpha)} \tag{44f}$$

The last formula (44f) is not obvious, but it is a result of the rhombohedral geometry of the unit cell. The second-to-last formula for the hexagonal close-packed unit cell arises from finding the area of a single isosceles triangle, then multiplying by the unit cell height.

One can plot the theoretical temperature T_C against the unit cell volume, and this is displayed in Figure 7.

In fact, there is a general trend, with increasing critical temperature as unit cell volume increases. But it is a very rough trend, with several outliers, namely V, Ta above the trend line, and Hf, Zr, and Ga below the trend line.

Nevertheless, these trends for T_C against atomic weight AW and against unit cell volume encourage us to do something similar for the higher T_C compound superconducting materials. Of course, the original high T_C materials were the YBCO [44-47] or ReBCO families (Re = rare-earth element). Cuprate superconductors are a family of high-temperature superconducting materials made of layers of copper oxides CuO_2 alternating with layers of other metal oxides, which act as charge reservoirs. Their superconducting properties are determined by electrons moving within weakly coupled copper-oxide CuO_2 layers, with neighboring layers containing ions such as La, Ba, Sr, or other atoms that act to stabilize the structures and dope electrons or holes onto the

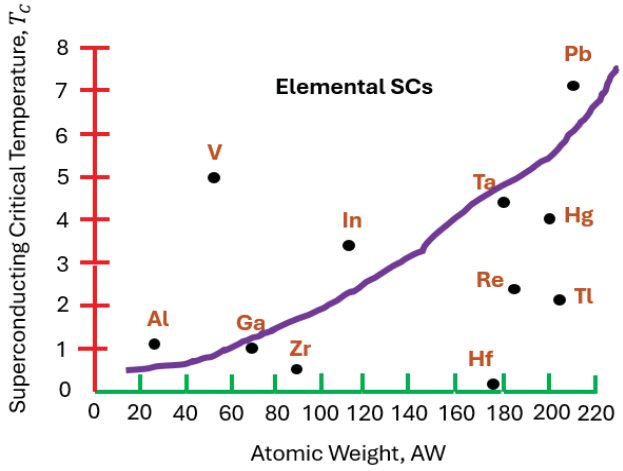

Figure 6: Superconducting elemental critical temperature versus elemental atomic weight.

Table 4: Elemental superconductors, their crystal structures, and lattice constants.

Element	Crystal Structure	Lattice Constants (Å)
Al, Aluminum	Face-centered cubic	a = 4.0493
Ga, Gallium	Orthorhombic base-centered	a = 4.5205, b = 7.6625, c = 4.5266
Hf, Hafnium	Hexagonal close-packed	a = 3.1942, c = 5.0512
Hg, Mercury	Rhombohedral	a = 3.0106, α = 70.529
In, Indium	Tetragonal body-centered	a = 3.2516, c = 4.9471
Pb, Lead	Face-centered cubic	a = 4.9499
Re, Rhenium	Hexagonal close-packed	a = 2.7610, c = 4.4584
Ta, Tantalum	Cubic body-centered	a = 3.3029
Tl, Thallium	Hexagonal close-packed	a = 3.4566, c = 5.5252
V, Vanadium	Cubic body-centered	a = 3.0272
Zr, Zirconium	Hexagonal close-packed	a = 3.2322, c = 5.1479

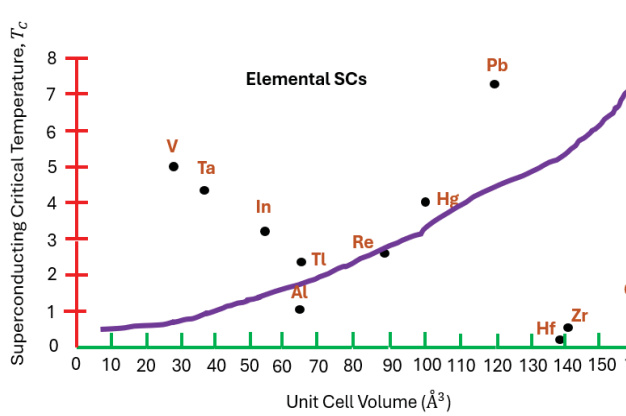

Figure 7: Critical superconducting temperature T_C against the unit cell volume given in Å^3.

Table 5: Elemental superconductors and their unit cell volumes.

Element	Unit cell volume $\psi_{m=-3} + \psi_{m=3}$
Al, Aluminum	66.40
Ga, Gallium	138.9
Hf, Hafnium	160.3
Hg, Mercury	23.49
In, Indium	52.31
Pb, Lead	121.2
Re, Rhenium	88.30
Ta, Tantalum	36.03
Tl, Thallium	66.01
V, Vanadium	27.74
Zr, Zirconium	139.7

copper-oxide layers. The undoped compounds are known as Mott insulators with long-range antiferromagnetic (AFM) order at sufficiently low temperatures.

There are other high T_C materials which are not in the YBCO or ReBCO families. This includes $HgBa_2Ca_{n-1}Cu_nO_{2n+\delta}$ with T_C = 133 – 138 K [26]. A superconductor containing both mercury and thallium is $Tl_{1.6}Hg_{0.4}Ba_2Ca_2Cu_3O_{10-\delta}$, which has a T_C = 130 K [48]. There are other Hg/Tl superconductors, a 1234 cuprate superconductor, like $Cu_{0.5}(Tl_{0.5-y}Hg_y)Ba_2Ca_3Cu_4O_{12-\delta}$, which has improved interlayer coupling [49]. Thallium-based SCs without mercury have a lower T_C [50,51]. The thallium family of high-temperature superconductors has the general formula $Tl_2Ba_2Ca_{n-1}Cu_nO_{2n+4+x}$. Generally, T_C increases with the number n of CuO_2 copper planes, peaking at n = 3. Another group of non-rare earth superconductors is the bismuth-strontium-calcium-copper-oxide family, $Bi_2Sr_2Ca_{n-1}Cu_nO_{2n+4+x}$ [52-57], with n = 2 being the most commonly studied family, although n = 1 and n = 3 have also been given attention too. Their T_c's are 107 – 160 K.

Cuprate superconductors are copper-oxide-based ceramic materials known for having the highest superconducting transition temperatures (T_C) at ambient pressure. The highest T_C values are generally found in materials with three or more copper-oxide (CuO_2) layers per unit cell.

Here are some of the most prominent cuprate superconductors with very high T_C:

1. Mercury-based cuprates (Hg-series)

These are considered the highest T_C materials at ambient pressure.

$HgBa_2Ca_2Cu_3O_{8+\delta}$: (Hg-1223); Currently holds the record for highest T_C at ambient pressure, with T_c≈134 K [26]. Under high pressure, this can increase to 164 K, which one wishes to avoid when trying to operate at standard conditions. Here δ indicates non-stoichiometric oxygen, which is essential to provide the necessary "holes" for superconductivity. It has a tetragonal crystal structure, $a=b=3.85\,\text{Å}, c=15.7\,\text{Å}$ [58,59]. Its unit cell volume is

$$V_{tetragonal}^{unit\ cell:\mathrm{HgBa2Ca2Cu3O8+\delta}} = a^2c = (3.85\,\text{Å})^2(15.7\,\text{Å}) = 232.7\,\text{Å}^3 \quad (45a)$$

$$N_{tetragonal}^{unit\ cell:\mathrm{HgBa2Ca2Cu3O8+\delta}} = 16 \quad (45b)$$

$HgBa_2CaCu_2O_6$(Hg-1212): T_C ≈128 K [60].

$HgBa_2CuO_4$(Hg-1201): T_C ≈94 K [61].

2. Thallium-based cuprates (Tl-series)

$Tl_2Ba_2Ca_2Cu_3O_{10}$ (Tl-2223): T_C ≈125 K [62].

It has a face-centered tetragonal crystal structure, $a=b=3.85\,\text{Å}, \langle c\rangle = 35.78\,\text{Å}$. Its unit cell volume is

$$V_{tetragonal;face-centered}^{unit\ cell:\mathrm{Tl2Ba2Ca2Cu3O10}} = a^2c = (3.85\,\text{Å})^2(35.78\,\text{Å}) = 530.35\,\text{Å}^3 \quad (46a)$$

$$N_{tetragonal;face-centered}^{unit\ cell:\mathrm{Tl2Ba2Ca2Cu3O10}} = 19 \quad (46b)$$

$TlBa_2Ca_3Cu_4O_{11}$ (Tl-1234): T_C ≈122 K [63]. The structure is tetragonal, with four CuO_2 layers, with lattice constants a = 3.85 Å and c = 19.1 Å.

$Tl_2Ba_2CaCu_2O_8$ (Tl-2212): T_C ≈108 K.

3. Bismuth-based cuprates (BSCCO)

$Bi_2Sr_2Ca_2Cu_3O_{10}$ (Bi-2223): T_C ≈110 K [64].

It has a body-centered tetragonal crystal structure, $\langle a\rangle = \langle b\rangle = 3.835\,\text{Å}, \langle c\rangle = 36.9\,\text{Å}$. Its unit cell volume is

$$V_{tetragonal;body-centered}^{unit\ cell:\mathrm{Bi2Sr2Ca2Cu3O10}} = a^2c = (3.835\,\text{Å})^2(36.9\,\text{Å}) = 542.70\,\text{Å}^3 \quad (47a)$$

$$N_{tetragonal;body-centered}^{unit\ cell:\mathrm{Bi2Sr2Ca2Cu3O10}} = 19 \quad (47b)$$

$Bi_2Sr_2CaCu_2O_8$(Bi-2212): T_C ≈85 K [65-70].

4. Rare-Earth Barium Copper Oxides (ReBCO)

$YBa_2Cu_3O_7$ (YBCO): T_C ≈92 K. This was the first material found to superconduct above the liquid nitrogen temperature (77 K), with the rare-earth element being Re = Y. It has an orthorhombic crystal structure, $a=3.82\,\text{Å}, b=3.89\,\text{Å}, c=11.67\,\text{Å}$ [71]. When the oxygen content changes, that is the doping to induce either holes or electrons as the conducting carriers, by changing O_7 to $O_{7-\delta}$ with δ > 0.6, which makes a shortage of oxygen, and a small positive pool of carriers (holes), then the crystal structure changes from orthorhombic to tetragonal. Its unit cell volume will be

$$V_{orthorhombic,}^{unit\ cell;\mathrm{YBa2Cu3O7}} = abc = (3.82\,\text{Å})(3.89\,\text{Å})(11.67\,\text{Å}) = 173.4\,\text{Å}^3 \quad (48a)$$

$$N_{orthorhombic}^{unit\ cell:YBCO} = 13 \quad (48b)$$

Critical superconducting temperature versus unit cell volume can be plotted, and is shown in Figure 8, using the equation results seen in (45a), (46a), (47a), and (48a).

One concludes from inspection of Figure 8 (look at the purple curve) that there is no marked association between T_C and increasing unit cell volume. However, there is a trend (green curve) for the rare-earth and mercury-based superconductors to have increasing T_C with increasing unit

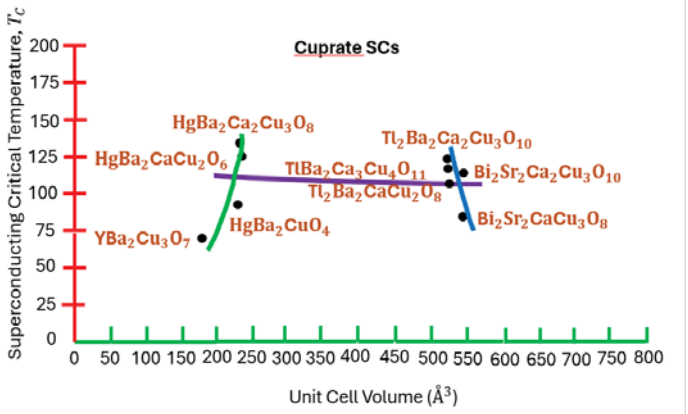

Figure 8: Cuprate superconductors giving T_C *vs.* unit cell volume (Å^3). Shown are mercury-, thallium-, bismuth-, and rare-earth- based compounds.

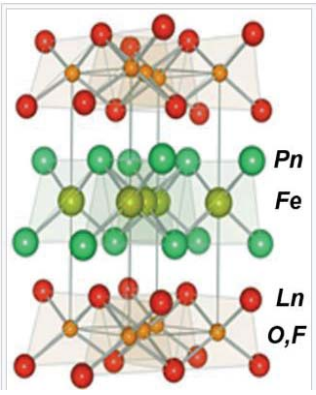

Figure 9: Crystal unit cell structure of a LnFeAsOF class of 1111-type of ferropnictides, where Ln = a lanthanide series element, Ln = La, Ce, Pr, Nd, Pm, Sm, Eu, Gd, Tb, Dy, Ho, Er, Tm, Yb, Lu. Pnictide elements are Pn = N, P, As, Sb, Bi, Mc [77].

cell volume. For thallium and bismuth-based superconductors, there is a reverse trend for decreasing T_C with increasing unit cell volume. These two counter trends are what generate the lack of any general apparent trend.

Iron pnictides have relatively high T_C's too. And they are thought to give a perspective on non-BCS mechanisms, so they have been extensively investigated. Figure 9 provides the unit cell crystal structure of 1111-type ferropnictide.

Iron-based superconductors of the group of oxypnictides were initially called ferropnictides. The crystal structure of these compounds displays conducting layers of iron and a pnictogen (typically arsenic (As) and phosphorus (P)) separated by a charge-reservoir block [8]. It has also been found that some iron chalcogens and crystallogens superconduct.

Iron-based superconductors are classified according to their crystal structure and chemical formula into the following main families.

A. 1111-type, with representative compounds LaFePO, LaFeAsO, SmFeAsO, PrFeAsO, and LaFeSiH

Let's find the unit cell volume of LaFePO [72-76]. Its crystallographic dimensions are for its tetragonal structure $\langle a\rangle = \langle b\rangle = 4.005\,\text{Å}$, $\langle c\rangle = 8.796\,\text{Å}$, with alternating layers of La-O and Fe-P stacked along the c-axis. Bond lengths are $d_{La-P}^{\text{LaFePO}} = 3.40\,\text{Å}$, $d_{La-O}^{\text{LaFePO}} = 2.38\,\text{Å}$, and $d_{Fe-P}^{\text{LaFePO}} = 2.53\,\text{Å}$.

$$V_{tetragonal}^{unit\ cell:\text{LaFePO}} = a^2c = \left(4.005\,\text{Å}\right)^2\left(8.796\,\text{Å}\right) = 141.09\,\text{Å}^3 \quad (49a)$$

$$N_{tetragonal}^{unit\ cell:\text{LaFePO}} = 4 \quad (49b)$$

Its T_C = 4 - 7 K.

For LaFeAsO, it is not superconducting, has AFM ordering, and is a semimetal. But doping with fluorine, or hydrogen, changes that [77-85]. For $LaFeAsO_{1-x}F_x$, and x = 0.1, it has $T_C \approx$ 26 K and a single domed behavior with the AFM ordering suppressed. For $LaFeAsO_{1-x}H_x$. It has $T_C \approx$ 36.5 K. Lattice parameters are $\langle a\rangle = \langle b\rangle = 4.035\,\text{Å}, \langle c\rangle = 8.746\,\text{Å}$. Therefore, its unit cell volume is

$$V_{tetragonal}^{unit\ cell:\text{LaFeAsO}} = a^2c = \left(4.035\,\text{Å}\right)^2\left(8.746\,\text{Å}\right) = 142.40\,\text{Å}^3 \quad (50a)$$

$$N_{tetragonal}^{unit\ cell:\text{LaFeAsO}} = 4 \quad (50b)$$

There are two superconducting domes are seen with H doping, an x range of 0.08 < x < 0.1. For a T_C versus x doping plot, first dome occurs at 0.08 < x < 0.1 with $T_C \approx$ 26 - 29 K, and second dome occurs at 0.3 < x < 0.35 with $T_C \approx$ 36 - 37 K. What is happening here is that the H anion H^- replaces the O anion O^{2-}, releasing an electron for conductivity (of course, pairing is required in actual superconductive transport since the basic unit of charge for superconductivity is $2e^-$).

For SmFeAsO, the key is to dope with either fluorine or hydrogen atoms [86,87]. For using F doping, the highest T_C = 55 K occurs for $SmFeAsO_{0.8}F_{0.2}$. (Note that $NdFeAsO_{1-x}F_x$ has also been found to have a similar T_C). It has unit cell dimensions of $a = b = 3.93\,\text{Å}, c = 8.48\,\text{Å}$. .

$$V_{tetragonal}^{unit\ cell:\text{SmFeAsO0.8F0.2}} = a^2c = \left(3.93\,\text{Å}\right)^2\left(8.48\,\text{Å}\right) = 130.97\,\text{Å}^3 \quad (51a)$$

$$N_{tetragonal}^{unit\ cell:\text{SmFeAsO0.8F0.2}} = 4 \quad (51b)$$

Using hydrogen doping, $SmFeAsO_{1-x}H_x$, T_C = 55 - 58 K, where $0.07 < x < 0.16$. Lattice parameters are

$$\langle a\rangle = \langle b\rangle = 3.918\,\text{Å}, \langle c\rangle = 8.441\,\text{Å}.$$

$$V_{tetragonal}^{unit\ cell:\text{SmFeAsO1-xHx}} = a^2c = \left(3.918\,\text{Å}\right)^2\left(8.441\,\text{Å}\right) = 129.58\,\text{Å}^3 \quad (52a)$$

$$N_{tetragonal}^{unit\ cell:\text{SmFeAsO1-xHx}} = 4 \quad (52b)$$

What is special about these 1111-type superconductors is that they have high upper critical fields $\mu_0 H_{c2}$ exceeding 100 T.

For PrFeAsO, superconductivity results from doping, suppressing the AFM spin density wave (SDW) [88–94]. Its lattice dimensions are a = b = 3.98 Å, c = 8.65 Å. Its unit cell volume is

$$V_{tetragonal}^{unit\ cell:\mathrm{PrFeAsO}} = a^2 c = (3.98\,Å)^2 (8.65\,Å) = 137.02\,Å^3 \quad (53a)$$

$$N_{tetragonal}^{unit\ cell:\mathrm{PrFeAsO}} = 4 \quad (53b)$$

Under doped PrFeAsO using F doping to reduce O atoms yields $PrFeAsO_{0.7}F_{0.3}$ and a T_C = 25.2 K. Reducing O content slightly and reducing F further to cause an atom imbalance gives $PrFeAsO_{0.65}F_{0.15}$ with T_C = 47 - 52 K. An interesting observation is that replacing the La atom (radius 1.87 Å) with the smaller radius Pr atom (radius 1.82 Å), induces a sort of "chemical pressure" due to the 2.7% radaii reduction.

For LaFeSiH [95–99], lattice dimensions are $a = b = 4.027$ Å, $c = 8.037$ Å. Its unit cell volume is

$$V_{tetragonal}^{unit\ cell:\mathrm{LaFeSiH}} = a^2 c = (4.027\,Å)^2 (8.037\,Å) = 130.33\,Å^3 \quad (54a)$$

$$N_{tetragonal}^{unit\ cell:\mathrm{LaFeSiH}} = 4 \quad (54b)$$

Its iron-silicon atom height separation is $d_{Fe-Si} = 1.20\,Å$. And its T_C = 10 K.

B. 111-type such as LiFeAs, NaFeAs, and LiFeP

LiFeAs has a T_C = 18 K, tetragonal crystal structure, with lattice dimensions of $a = b = 3.7914$ Å, $c = 6.364$ Å [100,101], with multiple nodeless superconducting (SC) gaps with $2\Delta/k_BT_c$ ratios varying from 2.8 to 6.4, depending on the Fermi surface (FS) [102]. The superfluid density $p_s(T)=\lambda^2(0)/\lambda^2(T)$ is well described by the self-consistent two-gap γ model [103]. Its 3D electronic has been examined [104]. Using density functional theory (DFT) and functional renormalization group method, the superconducting order parameter is found to be of s+- type driven by collinear antiferromagnetic fluctuations, with the parent compound displaying no magnetic order, but superconductivity [105]. Superconducting pnictides are widely found to feature spin-singlet pairing in the vicinity of an antiferromagnetic phase; however, in LiFeAs, a study shows antiferromagnetic order to be absent and almost ferromagnetic fluctuations, which drive an instability toward spin-triplet p-wave superconductivity [106]. However, the system can be tuned toward a spin-density-wave (SDW) quantum-critical point, showing that LiFeAs is a strongly correlated system and its superconductivity is likely from the SDW fluctuations [106]. Its unit cell volume will then be

$$V_{tetragonal}^{unit\ cell:\mathrm{LiFeAs}} = a^2 c = (3.791\,Å)^2 (6.364\,Å) = 91.46\,Å^3 \quad (55a)$$

$$N_{tetragonal}^{unit\ cell:\ \mathrm{LiFeAs}} = 3 \quad (55b)$$

For NaFeAs, its T_C = 4 - 25 K, tetragonal crystal structure, with lattice dimensions of $a = b = 3.947$ Å, $c = 6.991$ Å. It typically exhibits a tetragonal-to-orthorhombic phase transition ($T_{phase}^{Tetra\to ortho} \approx 53-58\,K$ and a collinear antiferromagnetic (SDW) transition ($T_{SDW}^{coll\ AFM} \approx 40-45\,K$), and coexistence of superconductivity and magnetic ordering [107]. It was found in another study that this compound is found to undergo three successive phase transitions at around 52, 41, and 23 K, which correspond to structural, magnetic, and superconducting transitions, respectively, and the Hall effect indicates an energy gap at low temperature due to the occurrence of spin-density-wave instability, giving direct experimental evidence of the magnetic ordering in the nearly stoichiometric NaFeAs [108]. Angle-resolved photoemission spectroscopy (ARPES) is used to study twinned and detwinned iron pnictide compound NaFeAs, with distinct signatures of electronic reconstruction (orbital anisotropy in d_{xy} and d_{yz} bands), and observed to occur at the structural (T_S) and magnetic (T_{SDW}) transitions, with implications for observance of nematic electronic phase in iron pnictides [109]. Another ARPES study looked at k_z band dispersions and d_{z^2} orbital [110]. 3D electronic structure of the nematic and antiferromagnetic phases of NaFeAs has been investigated [111], as well as electron nematicity and unidirectional antiferroic fluctuations [112]. Numerical LDA+DMFT calculations compared with ARPES data show that effective mass renormalization near the Fermi level is of order m*/3, due to Fe 3d orbital correlation effects without boson mode effects [113]. Its unit cell volume will then be

$$V_{tetragonal}^{unit\ cell:\mathrm{NaFeAs}} = a^2 c = (3.947\,Å)^2 (6.991\,Å) = 108.91\,Å^3 \quad (56a)$$

$$N_{tetragonal}^{unit\ cell:\mathrm{NaFeAs}} = 3 \quad (56b)$$

For LiFeP, its T_C = 4 - 25 K, tetragonal crystal structure, with lattice dimensions of $a = b = 3.692$ Å, $c = 6.031$ Å. Original discovery, see [114]. There is a change in the topology of the Fermi surface where a hole pocket with Fe d_{z^2} orbital character changes its geometry from a closed shape in the local-density approximation to an open shape upon inclusion of correlations - low T_C and the nodal gap observed in these materials relates this [115]. The discontinuity in the specific heat ΔC at T_C violates the global trend in $\Delta C/T_C$ with T_C [116]. Using DFT to obtain electronic DOS, overlapping of bands near the Fermi level (3s p state far below E_F, 3d Fe state near E_F, and Li above E_F) shows the metallic nature of LiFeP [117]. Its unit cell volume will then be

$$V_{tetragonal}^{unit\ cell:\mathrm{LiFeP}} = a^2 c = (3.692\,Å)^2 (6.031\,Å) = 82.21\,Å^3 \quad (57a)$$

$$N_{tetragonal}^{unit\ cell:\mathrm{LiFeP}} = 3 \quad (57b)$$

C. 11-type FeSe

A key observation is that the clean superconducting phase for FeSe exists only in those samples prepared with intentional Se deficiency [118,119]. It shows a spin-density wave (SDW) ground state [120]. This superconductor has a T_C = 8 - 9 K, tetragonal crystal structure, with lattice dimensions of $\langle a\rangle = \langle b\rangle = 3.765Å$, $\langle c\rangle = 5.50Å$. Its unit cell volume will then be

$$V_{tetragonal}^{unit\ cell:\mathrm{FeSe}} = a^2 c = (3.765\,Å)^2 (5.50\,Å) = 77.96\,Å^3 \quad (58a)$$

$$N_{tetragonal}^{unit\ cell:\mathrm{FeSe}} = 2 \quad (58b)$$

The binary compound FeSe has the ability to reach a T_C over 65 K in monolayer films on substrates like $SrTiO_3$. This may be of more than passing interest if there were a way to use this

fact by fabricating stacked binary SC-perovskite sandwiches into conducting wires for grid power movement.

D. 122-type such as $BaFe_2As_2$, $SrFe_2As_2$ and $CaFe_2As_2$

$BaFe_2As_2$ does not display superconductivity in its pure form, but only with a fourth elemental doping, such as K atom doping to generate holes, giving $Ba_{1-x}K_xFe_2As_2$ with a T_C = 38 K for x = 0.4 [121], or Co atom doping generating electrons, yielding $BaFe_{2-x}Co_xAs_2$ with a T_C = 22 K for x = 0.2 [122]. Density functional theory (DFT) calculations have been performed on this material [123]. Achieving high critical current densities J_C can be attained by removing nano-cracks at grain boundaries [124]. Ni_x doping has also been done, giving $BaFe_{2-x}Ni_xAs_2$ with a maximum of 20.5 K at x = 0.096 [125]. Annealing can raise T_C [126]. Lattice parameters are $a = b = 3.96$ Å, $c = 13.01$ Å.

$$V_{tetragonal}^{unit\ cell:BaFe2As2} = a^2c = (3.96\,Å)^2(13.01\,Å) = 201.0\,Å^3 \quad (59a)$$

$$N_{tetragonal}^{unit\ cell:BaFe2As2} = 5 \quad (59b)$$

$SrFe_2As_2$ also does not yield superconductivity in its pure form, but only with a fourth elemental doping, such as K atom doping (x = 0.4) to generate holes or seen even higher doping x = 0.5 – 0.6 for K or Cs doping [127,128], giving $Sr_{1-x}K_xFe_2As_2$ with a T_C = 37 - 38 K, or Co atom doping (x = 0.2) generating electrons, yielding $SrFe_{2-x}Co_xAs_2$ with a T_C = 20 K [129]. Lattice parameters are $a = b = 3.925$ Å, $c = 12.35$ Å.

$$V_{tetragonal}^{unit\ cell:SrFe2As2} = a^2c = (3.925\,Å)^2(12.35\,Å) = 190.26\,Å^3 \quad (60a)$$

$$N_{tetragonal}^{unit\ cell:SrFe2As2} = 5 \quad (60b)$$

Finally, $CaFe_2As_2$ does not yield superconductivity in its pure form, but only with a fifth rare-earth elemental doping, such as Re = La, Ce, Pr atom doping, with Pr doping (x = 0.1) $Ca_{1-x}Pr_xFe_2As_2$, and the highest T_C = 49 K [130]. Lattice parameters in this collapsed tetragonal state are $a = b = 3.97$ Å, $c = 10.61$ Å (down from the ambient value of $c = 11.69$ Å).

$$V_{tetragonal}^{unit\ cell:CaFe2As2} = a^2c = (3.97\,Å)^2(10.61\,Å) = 167.22\,Å^3 \quad (61a)$$

$$N_{tetragonal}^{unit\ cell:CaFe2As2} = 5 \quad (61b)$$

Note here that talking about pnictides using externally applied pressure to elevate T_C is not done to prepare HTC superconductors for ready application in grid power lines, because one desires room temperature operation under standard conditions, which means no use of high pressures.

Compared with other families, the synthesis of the 122 compounds is relatively easy, which facilitates the investigation of these systems.

E. 42622-type such as $Ca_4Al_2O_6Fe_2As_2$ and 32522-type such as $Ca_3Al_2O_5Fe_2As_2$

$Ca_4Al_2O_6Fe_2As_2$ requires doping to give $Ca_4Al_2O_{6-y}Fe_2As_2$ and is of the general class Al-42622(*Pn*), $Ca_4Al_2O_{6-y}Fe_2(Pn)_2$, where *Pn* = As, P [131,132]. These new materials are synthesized by using the high-pressure synthesis method. Al-42622 shows a superconducting critical temperature T_c at 28.3 K for *Pn* = As and 17.1 K for *Pn* = P. It is well-known that the Fe–As layers responsible for superconductivity create the charge carriers and transfer them to the perovskite blocking layers. Within the series of blocking layers, T_c strongly depends on the crystal structure parameter such as the As–Fe–As tetrahedron bond angle α. Replacement of key atoms by smaller ionic radius atoms causes considerable shrinkage in the lattice constant making α approach the regular ideal tetrahedron angle α = 109.5°, resulting in emergence of superconductivity with T_c becoming a maximum when As–Fe–As α approaches 109.5°. The lattice parameters of Al-42622(Pn) are a = 3.713 Å, c = 15.407 Å, and a = 3.692 Å, c = 14.934 Å for Pn = As and P, respectively, are the smallest among the iron-pnictide superconductors. Correspondingly, Al-42622(As) has the smallest As–Fe–As bond angle α = 102.1° and the largest As distance from the Fe planes $d_{As\text{-}Fe}$ = 1.5 Å.

Unit cell volume for a tetrahedron requires knowledge of lattice dimensions a and c. It is given by

Thus, for Pn = As,

$$V_{tetragonal}^{unit\ cell:Ca4Al2O5Fe2(Pn=As)2} = (3.713\ Å)^2(15.407\ Å) = 212.41\,Å^3 \quad (62a)$$

$$N_{tetragonal}^{unit\ cell:Ca4Al2O5Fe2(Pn=As)2} = 15 \quad (62b)$$

When Pn = P,

$$V_{tetragonal}^{unit\ cell:Ca4Al2O5Fe2(Pn=P)2} = (3.692\ Å)^2(14.934\ Å) = 203.56\,Å^3 \quad (63a)$$

$$N_{tetragonal}^{unit\ cell:Ca4Al2O5Fe2(Pn=P)2} = 15 \quad (63b)$$

$Ca_3Al_2O_5Fe_2As_2$, which again is synthesized by using the high-pressure method, and requires doping to give superconductivity as $Ca_3Al_2O_{5-y}Fe_2As_2$, and is of the general class Al-32522(*Pn*), where *Pn* = As, P. Al-32522(*Pn*) shows a T_c at 30.2 K for *Pn* = As and 16.6 K for *Pn* = P [133].

Figure 10 gives the pnictide superconductor T_C versus unit cell volume.

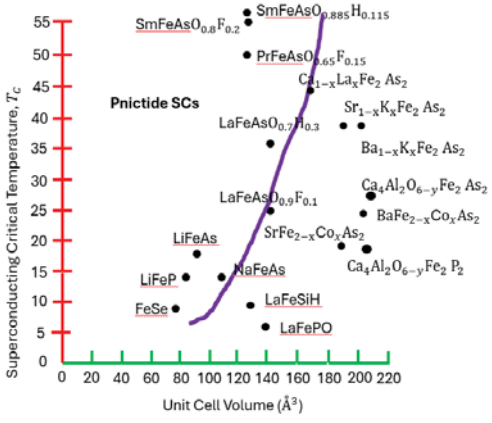

Figure 10: Shows the pnictide superconductor T_c versus unit cell volume (Å).

One concludes from inspection of Figure 10 that there is a rough increase in T_C with increasing unit cell volume.

VII. Discussion

Much can be discerned from examination of the elemental superconducting materials, cuprate high-temperature superconducting materials, and the pnictide superconducting materials. Especially remarkable is the maximum T_C seen for the pnictide SC materials, which is roughly $T_C^{pnictide}\Big|_{max} \approx 50K$. Since the consensus, looking at all of the literature in the pnictide SC area, seems to be that there is a non-BCS mechanism responsible for the superconductivity, likely a spin-mediated anti-ferromagnetic phenomenon, the contribution based on additive Hamiltonian matrix elements, would be to utilize (43), and break out each mechanism contribution to the critical SC temperature

$$T_C^{max} = \sum_m T_C^m ; T_C^m = \frac{\langle \alpha_m \rangle}{\pi} \frac{\hbar \omega_m}{k_B} \tag{62}$$

Here, the summation is over all energy exchange mechanisms contributing to the Hamiltonian. Equation (62) is very telling. It says that it may be very likely that each mechanism contributing to T_C gives about 50 K toward upping the critical temperature.

Now turn attention to the element SCs. There we saw that $T_C^{elemental}\Big|_{max} \approx 10K$. It is known that electron-phonon energy exchange is responsible for this superconductivity. This is the conventional superconductivity, known as the BCS type of superconductivity. Let's be generous and identify the maximum BCS type of superconductivity as $T_C^{BCS}\Big|_{max} \approx 50K$. This then gives us insight into understanding the original of the maximum, under standard conditions, for cuprate SCs, which is on the order of $T_C^{cuprate}\Big|_{max} \approx 150K$. Because it is understood from the literature that charge density waves (CDW) may be active in curate SCs, and spin density waves (SDW) have also been identified, this may be all that is necessary to explain the highest seen of all superconducting material T_C's in cuprates, once one accepts the likely possibility that BCS type of conventional superconductivity is also contributing to T_C. Thus, for cuprate SCs, the equation for T_C is

$$T_C^{max} = \sum_{m=BCS,SDW,CDW} T_C^m = 3 \times (50K) = 150K \tag{63}$$

The next question, given the understanding gained from these arguments, is how to elevate the T_C toward room temperature operation. Clearly, three other mechanisms must be found if one associates a maximum contributing T_C^m of 50 K, recognizing that standard room temperature conditions are associated with a temperature of $T_{rm}^{stand} = 293.15K\ (20C = 68F)$. But one may also use other temperatures as a reference, such as $T_{rm}^{stand} = 298.15K\ (25C = 77F)$. An approximation to any of these chosen standard-like conditions would be to use 300 K, and that gives us

$$\frac{T_{rm}^{stand}}{T_C^{max}} \approx 2 \tag{64}$$

VIII. Conclusion

This presentation has covered the quantum wave nature of the superconducting electrons, the 3D crystal lattice effect on the quantum wavefunction pairing overlap, orbital spatial characteristics, and the energy exchange mechanisms relationship to the critical superconducting temperature T_C. Shown also are the trends for elemental, cuprate, and pnictide superconductors.

It has been discovered that tractable relationships can be derived that relate the energy exchange mechanisms to T_C. Forecasting which new solid-state chemical compounds will yield much higher results and lead to practical implementation is a very difficult problem. However, in our treatment, how potential energy exchange mechanisms may contribute to both the Hamiltonians and the mechanism critical T_C^m's, provides a way forward to elevate the superconducting critical temperature to room temperature.

References

1. Krowne CM. Microscopic quantum mechanical Marcus theory for chemical reactions and its relationship to the Butler-Volmer equation used in redox flow battery analysis. Int J Quantum Chem. 2024;124(1). Available from: https://doi.org/10.1002/qua.27279
2. Krowne CM. Nernst equations and concentration chemical reaction over potentials for VRFB operation. J Electrochem Soc. 2023;170:100534. Available from: https://doi.org/10.1149/1945-7111/ad0073
3. Krowne CM. Analytical current-voltage formulas in electrodes and concentration differences for VRFB. Electrochim Acta. 2024;476:143709. Available from: https://doi.org/10.1016/j.electacta.2023.143709
4. Krowne CM. Physics, electrochemistry, chemistry, and electronics of the vanadium redox flow battery by analyzing all the governing equations. Phys Chem Chem Phys. 2024;26:2823-2862. Available from: https://pubs.rsc.org/en/content/articlelanding/2024/cp/d3cp04223e
5. Krowne CM. Spatial distribution of pressure using fluid physics for the vanadium redox flow battery and minimizing fluid crossover between the battery electrodes. J Electrochem Soc. 2024;171:020537. Available from: https://doi.org/10.1149/1945-7111/ad2734
6. Krowne CM. Fluid physics impacting the vanadium and other redox flow batteries. J Electrochem Soc. 2024;171:060517. Available from: https://doi.org/10.1149/1945-7111/ad5252
7. Krowne CM. Determination of the ion concentrations in VRFB by non-invasive optical techniques due to chemical reactions, complexes and side reactions. J Electrochem Soc. 2024;171:020546. Available from: https://doi.org/10.1149/1945-7111/ad2818
8. Krowne CM. Measures of performance of the vanadium and other redox flow batteries. J Electrochem Soc. 2024;171:050538. Available from: https://doi.org/10.1149/1945-7111/ad4824
9. Krowne CM. State of charge (SoC) of the vanadium and other redox flow batteries: identification of the electrode and bipolar plate contributions. J Electrochem Soc. 2024;171:100523. Available from: https://doi.org/.1149/1945-7111/ad80d4
10. Krowne CM. Charging electrochemistry, electronics and fluid requirements for redox flow batteries. J Electrochem Soc. 2025;172:100525. Available from: https://doi.org/:10.1149/1945-7111/ae0f5a

11. Daniel M, Byron NP, Krowne CM. Harnessing redox flow batteries for industrial applications: opportunities and future directions. J Power Sources. 2023;591:233889. Available from: https://doi.org/10.1016/j.jpowsour.2023.233889

12. Kamihara Y, Hiramatsu H, Hirano M, Kawamura R, Yanagi H, Kamiya T, et al. Iron-based layered superconductor: LaOFeP. J Am Chem Soc. 2006;128(31):10012-10013. Available from: https://doi.org/10.1021/ja063355c

13. Kamihara Y, Watanabe T, Hirano M, Hosono H. Iron-based layered superconductor La[O1-xFx]FeAs (x = 0.05-0.12) with Tc = 26 K. J Am Chem Soc. 2008;130(11):3296-3297. Available from: https://doi.org/10.1021/ja800073m

14. Hosono H, Tanabe K, Takayama-Muromachi E, Kageyama H, Yamanaka S, Kumakura H, et al. Exploration of new superconductors and functional materials, and fabrication of superconducting tapes and wires of iron pnictides. Sci Technol Adv Mater. 2015;16(3):033503. Available from: https://doi.org/10.1088/1468-6996/16/3/033503

15. Yankowitz M, Chen S, Polshyn H, Zhang Y, Watanabe K, Taniguchi T, et al. Tuning superconductivity in twisted bilayer graphene. Science. 2019;363(6431):1059-1064. Available from: https://doi.org/10.1126/science.aav1910

16. Oh M, Nuckolls KP, Wong D, Lee RL, Liu X, Watanabe K, et al. Evidence for unconventional superconductivity in twisted bilayer graphene. Nature. 2021;600:240-245. Available from: https://doi.org/10.1038/s41586-021-04121-x

17. Su R, Kuiri M, Watanabe K, Taniguchi T, Folk JA. Superconductivity in twisted double bilayer graphene stabilized by WSe2. Nat Mater. 2023;22:1332-1337. Available from: https://doi.org/10.1038/s41563-023-01653-7

18. Nagamatsu J, Nakagawa N, Muranaka T, Zenitani Y, Akimitsu J. Superconductivity at 39 K in magnesium diboride. Nature. 2001;410(6824):63-64. Available from: https://doi.org/10.1038/35065039

19. Bud'ko SL, Canfield PC. Superconductivity of magnesium diboride. Physica C. 2015;514:142-151. Available from: https://doi.org/10.1016/j.physc.2015.02.024

20. Drozdov AP, Eremets MI, Troyan IA, Ksenofontov V, Shylin SI. Conventional superconductivity at 203 kelvin at high pressures in the sulfur hydride system. Nature. 2015;525:73-76. Available from: https://doi.org/10.1038/nature14964

21. Einaga M, Sakata M, Ishikawa T, Shimizu K, Eremets MI, Drozdov AP, et al. Crystal structure of the superconducting phase of sulfur hydride. Nat Phys. 2016;12:835-838. Available from: https://doi.org/10.1038/nphys3760

22. Bednorz JG, Müller KA. Possible high Tc superconductivity in the Ba-La-Cu-O system. Z Phys B. 1986;64(2):189-193. Available from: https://link.springer.com/article/10.1007/BF01303701

23. Buchanan M. Mind the pseudogap. Nature. 2001;409(6816):8-11. Available from: https://doi.org/DOI:10.1038/35051238

24. Wu MK, Ashburn JR, Torng CJ, Hor PH, Meng RL, Gao L, et al. Superconductivity at 93 K in a new mixed-phase Y-Ba-Cu-O compound system at ambient pressure. Phys Rev Lett. 1987;58(9):908-910. Available from: https://doi.org/10.1103/PhysRevLett.58.908

25. Sheng ZZ, Hermann AM. Bulk superconductivity at 120 K in the Tl-Ca/Ba-Cu-O system. Nature. 1988;332(6160):138-139. Available from: https://doi.org/10.1038/332138a0

26. Schilling A, Cantoni M, Guo JD, Ott HR. Superconductivity above 130 K in the Hg-Ba-Ca-Cu-O system. Nature. 1993;363(6424):56-58. Available from: https://doi.org/10.1038/363056a0

27. Lee PA. From high temperature superconductivity to quantum spin liquid: progress in strong correlation physics. Rep Prog Phys. 2008;71(1):012501. Available from: https://doi.org/10.48550/arXiv.0708.2115

28. Li X, Zou C, Ding Y, Yan H, Ye S, Li H, et al. Evolution of charge and pair density modulations in overdoped Bi2Sr2CuO6+δ. Phys Rev X. 2021;11(1):011007. Available from: https://doi.org/10.1103/PhysRevX.11.011007

29. Krowne CM. Examination of 2D hexagonal band structure from a nanoscale perspective for use in electronic transport devices. In: Advances in Imaging and Electron Physics. Vol. 210. Amsterdam: Elsevier Academic Press; 2019. p. 23-45.

30. Osofsky MS, Hernández-Hangarter SC, Nath A, Wheeler VD, Walton SG, Krowne CM, et al. Functionalized graphene as a model system for the two-dimensional metal-insulator transition. Sci Rep. 2016;6:19939. Available from: https://doi.org/10.1038/srep19939

31. Osofsky MS, Krowne CM, Charipar KM, Bussmann K, Chervin CN, Pala IR, et al. Disordered RuO2 exhibits two-dimensional, low-mobility transport and a metal-insulator transition. Sci Rep. 2016;6:21836. Available from: https://www.nature.com/articles/srep21836

32. Krowne CM, Sha X. Atomic structural and electronic bandstructure calculations for borophene. Mater Res Express. 2021;8:026301. Available from: https://doi.org/10.1088/2053-1591/abdf7e?urlappend=%3Futm_source%3Dresearchgate.net%26utm_medium%3Darticle

33. Sha X, Krowne CM. First-principles quantum calculations for graphyne for electronic devices. Nanoscale Adv. 2021;3:5853-5859. Available from: https://doi.org/10.1039/D1NA00336D

34. Osofsky MS, Krowne CM, Soulen RJ Jr, Clements E, Woods G, Srikanth H, et al. New approaches for enhancing Tc. In: Proceedings of the 11th International Conference on Ceramic Materials and Components for Energy and Environmental Applications (CMCEE); 2015 Jun 14-19; Vancouver, Canada. Westerville (OH): American Ceramic Society; 2015.

35. Osofsky MS, Prestigiacomo JC, Krowne CM, Soulen RJ Jr, Kim H, Clements E, et al. Superconductivity near the metal-insulator transition. In: Electronic Materials and Applications Conference (EMA 2016); 2016 Jan 20-22; Orlando, FL. Westerville (OH): American Ceramic Society; 2016.

36. Osofsky MS, Prestigiacomo JC, Krowne CM, Soulen RJ Jr, Clements E, Woods G, Srikanth H, Takeuchi I. Superconductivity near the metal-insulator transition. In: 2016 MRS Spring Meeting & Exhibit; 2016 Mar 28-Apr 1; Phoenix, AZ. Warrendale (PA): Materials Research Society; 2016.

37. Smolyaninova VN, Korzi W, Yong G, Valente-Feliciano AM, Beverstock DR, Prestigiacomo JC, et al. Effect of metamaterial engineering on the superconductive properties of ultrathin layers of NbTiN. J Appl Phys. 2021;130:073901. Available from: https://misportal.jlab.org/sti/publications/16589/attachments/1699/Effect%20of%20metamaterial%20engineering%20on%20the%20superconductive%20properties%20of%20ultrthin%20layers%20of%20NbTiN.pdf

38. Krowne CM. Nanowire and nanocable junction capacitances: results for metal and semiconducting oxides. Phys Lett A. 2010;374:1172-1179. Available from: https://doi.org/10.1016/j.physleta.2009.12.056

39. Martinez JI, Calle-Vallejo F, Krowne CM, Alonso JA. First-principles structural and electronic characterization of ordered SiO2 nanowires. J Phys Chem C. 2012;116:18973-18982. Available from: https://doi.org/10.1021/jp3009223

40. Martinez JI, Abad E, Calle-Vallejo F, Krowne CM, Alonso JA. Tailoring structural and electronic properties of RuO2 nanotubes: many-body approach and electronic transport. Phys Chem Chem Phys. 2013;15(35):14715-14722. Available from: https://doi.org/10.1039/C3CP52092G

41. Cohen-Tannoudji C, Diu B, Laloe F. Quantum Mechanics. Vols. I-II. New York: Wiley; 1977.

42. Krowne CM. Disorder modifications of the critical temperature for superconductivity: a perspective from the point of view of nanoscience. In: Advances in Imaging and Electron Physics. Vol. 202. Amsterdam: Elsevier; 2017. p. 39-74.

43. Krowne CM. Critical magnetic field and its slope, specific heat, and gap for superconductivity as modified by nanoscopic disorder. In: Advances in Imaging and Electron Physics. Vol. 203. Amsterdam: Elsevier; 2017. p. 67-97. Available from: https://discovery.researcher.life/article/critical-magnetic-field-and-its-slope-specific-heat-and-gap-for-superconductivity-as-modified-by-nanoscopic-disorder/b467572108dc3a8fb60ad60f3f366841

44. Shekhter A, Ramshaw BJ, Liang R, Hardy WN, Bonn DA, Balakirev FF, et al. Bounding the pseudogap with a line of phase transitions in YBa2Cu3O6+δ Nature. 2013;498:75-77. Available from: https://doi.org/10.1038/nature12165

45. Kaiser S, Hunt CR, Nicoletti D, Hu W, Gierz I, Liu H, et al. Optically induced coherent transport far above Tc in underdoped YBa2Cu3O6+δ. Phys Rev B. 2014;89:184516. Available from: https://doi.org/10.1103/PhysRevB.89.184516

46. Kao YH, Yao YD, Jang LY, Xu F, Krol A, Song LW, et al. Effects of silver doping in the high-Tc superconductor system Y-Ba-Cu-O. J Appl Phys. 1990;67:353-361. Available from: https://doi.org/10.1063/1.345261

47. Tallon JL, Bernhard C, Shaked H, Hitterman RL, Jorgensen JD, et al. Generic superconducting phase behaviour in high-Tc cuprates: Tc variation with hole concentration in YBa2Cu3O7-δ. Phys Rev B. 1995;51(18):12911-12914. Available from: https://doi.org/10.1103/physrevb.51.12911

48. Goutenoire F, Maignan A, Van Tendeloo G, Martin C, Michel C, Hervieu M, et al. Substitution of mercury for thallium in the 2223-cuprate: the 130 K superconductor Tl1.6Hg0.4Ba2Ca2Cu3O10-δ. Solid State Commun. 1994;90(1):47-50. Available from: https://ui.adsabs.harvard.edu/abs/1994SSCom..90...47G/abstract

49. Mumtaz M, Khan NA, Khurram AA. Enhanced superconducting properties of Cu0.5(Tl0.5-yHgy)Ba2Ca3Cu4O12-δ (y = 0, 0.15, 0.25, 0.35) superconductor. J Alloys Compd. 2008;452(2):435-440. Available from: https://www.researchgate.net/publication/236152035_Enhanced_superconducting_properties_of_Cu0_5_Tl0_5-yHgy_Ba2Ca3Cu4O12-d_y

50. Sheng ZZ, Hermann AM, El Ali A, Almasan C, Estrada J, Datta T, et al. Superconductivity at 90 K in the Tl-Ba-Cu-O system. Phys Rev Lett. 1988;60(10):937-940. Available from: https://doi.org/10.1103/PhysRevLett.60.937

51. Sheng ZZ, Hermann AM. Superconductivity in the rare-earth-free Tl-Ba-Cu-O system above liquid-nitrogen temperature. Nature. 1988;332(6159):55-58. Available from: https://doi.org/10.1038/332055a0

52. Sunshine SA, Siegrist T, Schneemeyer LF, Murphy DW, Cava RJ, Batlogg B, et al. Structure and physical properties of single crystals of the 84-K superconductor Bi2.2Sr2Ca0.8Cu2O8+δ. Phys Rev B. 1988;38(1):893-896. Available from: https://doi.org/10.1103/PhysRevB.38.893

53. Subramanian MA, Torardi CC, Calabrese JC, Gopalakrishnan J, Morrissey KJ, Askew TR, et al. A new high-temperature superconductor: Bi2Sr3-xCaxCu2O8+y. Science. 1988;239(4843):1015-1017. Available from: https://doi.org/10.1126/science.239.4843.1015

54. Tallon JL, Buckley RG, Gilberd PW, Presland MR, Brown IWM, Bowd ME, et al. High-Tc superconducting phases in the series Bi2.1(Ca,Sr)n+1CunO2n+4+δ. Nature. 1988;333(6169):153-156. Available from: https://doi.org/10.1038/333153a0

55. Presland MR, Tallon JL, Buckley RG, Liu RS, Flower NE. General trends in oxygen stoichiometry effects on T_c in Bi and Tl superconductors. Physica C. 1991;176(1-3):95-105. Available from: https://ui.adsabs.harvard.edu/abs/1991PhyC..176...95P/abstract

56. Togano K. Properties of Pb-doped Bi-Sr-Ca-Cu-O superconductors. Appl Phys Lett. 1988;53(14):1329-1331. Available from: https://www.semanticscholar.org/paper/Magnetic-Properties-of-Pb-Doped-Bi-Sr-Ca-Cu-O-Kumakura-Togano/299d271b25dd1d470084c13eba5ef6961cd59094

57. Maeda H, Tanaka Y, Fukutumi M, Asano T. A new high-Tc oxide superconductor without a rare earth element. Jpn J Appl Phys. 1988;27(2). L209-L210. Available from: https://garfield.library.upenn.edu/classics1993/A1993KV05800001.pdf

58. Tokiwa-Yamamoto A, Isawa K, Itoh M, Adachi S, Yamauchi H. Composition, crystal structure and superconducting properties of Hg-Ba-Cu-O and Hg-Ba-Ca-Cu-O superconductors. Physica C. 1993;216(3-4):250-256.

59. Antipov EV, Loureiro SM, Chaillout C, Capponi JJ, Bordet P, Tholence JL, et al. The synthesis and characterization of the HgBa2Ca2Cu3O8+δ and HgBa2Ca3Cu4O10+δ phases. Physica C. 1993;215(1-2):1-10. Available from: https://ui.adsabs.harvard.edu/abs/1993PhyC..216..250T/abstract

60. Radaelli PG, Wagner JL, Hunter BA, Beno MA, Knapp GS, Jorgensen JD, et al. Structure, doping and superconductivity in HgBa2CaCu2O6+δ (Tc ≤128 K). Physica C. 1993;216(1-2):29-35. Available from: https://ui.adsabs.harvard.edu/abs/1993PhyC..216...29R/abstract

61. Putilin SN, Antipov EV, Chmaissem O, Marezio M. Superconductivity at 94 K in HgBa2CuO4+δ. Nature. 1993;362:226-228.

62. Ihara H, Sugise R, Hirabayashi M, Terada N, Jo M, Hayashi K, et al. A new high-Tc TlBa2Ca3Cu4O11 superconductor with Tc >120 K. Nature. 1988;334(6182):510-512. Available from: https://www.semanticscholar.org/paper/A-new-high-Tc-TlBa2Ca3Cu4O11-superconductor-with-Tc-Ihara-Sugise/ed0064745f75e3499a3e9af2c5f3dbed75c9d4bc

63. Torardi CC, Subramanian MA, Calabrese JC, Gopalakrishnan J, Morrissey KJ, Askew TR, et al. Crystal structure of Tl2Ba2Ca2Cu3O10, a 125 K superconductor. Science. 1988;240:631-634. Available from: https://doi.org/10.1126/science.240.4852.631

64. Lejay P, de Rango P, Sulpice A, Giordanengo B, Tournier R, Retoux R, et al. Superconductivity up to 110 K in Bi2Sr2Ca2Cu3O10 compounds. Rev Phys Appl. 1989;24:485-488. Available from: https://hal.science/jpa-00246071/document

65. Jacobs T. Unraveling the cuprate superconductor phase diagram: intrinsic tunneling spectroscopy and electrical doping [dissertation]. Stockholm (Sweden): Stockholm University; 2016. Available from: https://www.semanticscholar.org/paper/Unraveling-the-cuprate-superconductor-phase-diagram-Jacobs/450170d36488d0bb90d7fbd4b48fb65d8148e39b

66. Jacobs T, Katterwe SO, Motzkau H, Rydh A, Maljuk A, et al. Electron tunneling measurements of low-Tc single-layer Bi2+xSr2-yCuO6: evidence for a scaling disparity between superconducting and pseudogap states. Phys Rev B. 2012;86:214506. Available from: https://doi.org/10.1103/PhysRevB.86.214506

67. Motzkau H, Jacobs T, Katterwe SO, Rydh A, Krasnov VM. Persistent electrical doping of Bi2Sr2CaCu2O8+δ mesa structures. Phys Rev B. 2012;85:144519. Available from: https://doi.org/10.1103/PhysRevB.85.144519

68. Katterwe SO, Jacobs T, Maljuk A, Krasnov VM. Low anisotropy of the upper critical field in a strongly anisotropic layered cuprate: evidence for paramagnetically limited superconductivity. Phys Rev B. 2014;89:214516. Available from: https://doi.org/10.1103/PhysRevB.89.214516

69. Jacobs T, Simsek Y, Koval Y, Muller P, Krasnov VM. Sequence of Quantum Phase Transitions in Bi2Sr2CaCu2O(8+δ) Cuprates Revealed by In Situ Electrical Doping of One and the Same Sample. Phys Rev Lett. 2016;116:067001. Available from: https://doi.org/10.1103/PhysRevLett.116.067001

70. Jacobs T, Katterwe SO, Krasnov VM. Superconducting correlations above Tc in the pseudogap state of Bi2Sr2CaCu2O8+δ cuprates revealed by angular-dependent magnetotunneling. Phys Rev B. 2016;94:220501(R). Available from: https://doi.org/10.1103/PhysRevB.94.220501

71. Howe BA. Crystal structure and superconductivity of YBa2Cu3O7-x [master's thesis]. Mankato (MN): Minnesota State University; 2014. Available from: https://cornerstone.lib.mnsu.edu/cgi/viewcontent.cgi?article=1345&context=etds

72. Kamihara Y, Hiramatsu H, Kawamura R, Yanagi H, Kamiya T, Hosono H. Iron-based layered superconductor in LaOFeP. J Am Chem Soc. 2006;128:10012-10013. Available from: https://doi.org/10.1021/ja063355c

73. McQueen TM, Regulacio M, Williams AJ, Huang Q, Lynn JW, Hor YS, et al. Intrinsic properties of stoichiometric LaFePO. Phys Rev B. 2008;78(2):024521. Available from: https://doi.org/10.1103/PhysRevB.78.024521

74. Hamlin JJ, Baumbach RE, Zocco DA, Sayles TA, Maple MB. Superconductivity in single crystals of LaFePO. J Phys Condens Matter. 2008;20:365220. Available from: https://iopscience.iop.org/article/10.1088/0953-8984/20/36/365220

75. Sutherland M, Dunn J, Toews WH, O'Farrell E, Analytis JG, Fisher I, et al. Low-energy quasiparticles probed by heat transport in the iron-pnictide superconductor LaFePO. Phys Rev B. 2012;85(1):014517. Available from: https://doi.org/10.1103/PhysRevB.85.014517

76. Hicks CW, Lippman TM, Huber ME, Analytis JG, Chu JH, Erickson AS, et al. Evidence for a nodal energy gap in the iron-pnictide superconductor LaFePO from penetration depth measurements by scanning SQUID susceptometry. Phys Rev Lett. 2009;103(12):127003. Available from: https://doi.org/10.1103/PhysRevLett.103.127003

77. Kamihara Y, Watanabe T, Hirano M, Hosono H. Iron-based layered superconductor LaFeAsO1-xFx (x = 0.05-0.12) with Tc = 26 K. J Am Chem Soc. 2008;130(11):3296-3297. Available from: https://doi.org/10.1021/ja800073m

78. McGuire MA, Christianson AD, Sefat AS, Sales BC, Lumsden MD, Jin R, et al. Phase transitions in LaFeAsO: structural, magnetic, elastic, and transport properties, heat capacity and Mössbauer spectra. Phys Rev B. 2008;78:094517. Available from: https://doi.org/10.1103/PhysRevB.78.094517

79. Klingeler R, Leps N, Hellmann I, Popa A, Stockert U, Hess C, et al. Local antiferromagnetic correlations in the iron pnictide superconductors LaFeAsO1-xFx and Ca(Fe1-xCox)2As2 as seen via normal-state susceptibility. Phys Rev B. 2010;81:024506. Available from: https://doi.org/10.1103/PhysRevB.81.024506

80. Mazin II, Singh DJ, Johannes MD, Du MH. Unconventional superconductivity with a sign reversal in the order parameter of LaFeAsO1-xFx. Phys Rev Lett. 2008;101:057003. Available from: https://doi.org/10.1103/PhysRevLett.101.057003

81. Kuroki K, Onari S, Arita R, Usui H, Tanaka Y, Kontani H, et al. Unconventional pairing originating from the disconnected Fermi surfaces of superconducting LaFeAsO1-xFx. Phys Rev Lett. 2008;101:087004. Available from: https://doi.org/10.1103/PhysRevLett.101.087004

82. Haule K, Shim JH, Kotliar G. Correlated electronic structure of LaO1-xFxFeAs. Phys Rev Lett. 2008;100:226402. Available from: https://doi.org/10.1103/PhysRevLett.100.226402

83. Ahilan K, Ning FL, Imai T, Sefat AS, Jin R, McGuire MA, et al. 19F NMR investigation of the iron pnictide superconductor LaFeAsO0.89F0.11. Phys Rev B. 2008;78:100501. Available from: https://doi.org/10.1103/PhysRevB.78.100501

84. Sakurai R, Fujiwara N, Kawaguchi N, Yamakawa Y, Kontani H, Iimura S, et al. Quantum critical behavior in heavily doped LaFeAsO1-xHx pnictide superconductors analyzed using nuclear magnetic resonance. Phys Rev B. 2015;91:064509. Available from: https://doi.org/10.1103/PhysRevB.91.064509

85. Luetkens H, Klauss HH, Khasanov R, Amato A, Klingeler R, Hellmann I, et al. Field and temperature dependence of the superfluid density in LaFeAsO1-xFx superconductors: a muon spin relaxation study. Phys Rev Lett. 2008;101:097009. Available from: https://doi.org/10.1103/physrevlett.101.097009

86. Chen XH, Wu T, Wu G, Liu RH, Fang DF, Chen NL. Superconductivity at 43 K in SmFeAsO1-xFx. Nature. 2008;453:761-762. Available from: https://doi.org/10.1038/nature07045

87. Sanna S, De Renzi R, Lamura G, Ferdeghini C, Palenzona A, Putti M, et al. Magnetic-superconducting phase boundary of SmFeAsO1-xFx studied via muon spin rotation: unified behavior in a pnictide family. Phys Rev B. 2009;80:052503. Available from: https://doi.org/10.1103/PhysRevB.80.052503

88. McGuire MA, Hermann RP, Sefat AS, Sales BC, Jin R, Mandrus D, et al. Influence of the rare-earth element on the effects of the structural and magnetic phase transitions in CeFeAsO, PrFeAsO and NdFeAsO. New J Phys. 2009;11:025011. Available from: https://doi.org/10.1088/1367-2630/11/2/025011

89. Okazaki R, Konczykowski M, van der Beek CJ, Kato T, Hashimoto K, et al. Lower critical fields and the anisotropy in PrFeAsO1-y single crystals. Physica C. 2009;470(Suppl 1). S485-S486. Available from: https://doi.org/10.1016/j.physc.2009.12.041

90. Gretarsson H, Lupascu A, Kim J, Casa D, Gog T, Wu W, et al. Revealing the dual nature of magnetism in iron pnictides and iron chalcogenides using X-ray emission spectroscopy. Phys Rev B. 2011;84:100509. Available from: https://doi.org/10.1103/PhysRevB.84.100509

91. Nishi I, Ishikado M, Ideta S, Mataeb W, Yoshida T, Fujimori A, et al. Angle-resolved photoemission spectroscopy study of PrFeAsO0.7: comparison with LaFePO. Phys Rev B. 2011;84:014504. Available from: https://doi.org/10.1103/PhysRevB.84.014504

92. Shirai K, Kashiwaya H, Miura S, Ishikado M, Eisaki H, et al. Local transport properties of PrFeAsO0.7 using FIB micro-fabrication. Physica C. 2010;470(20):1473-1476. Available from: https://doi.org/10.1016/j.physc.2010.05.141

93. Bhoi D, Mandal P, Choudhury P. Vortex dynamics and second magnetization peak in PrFeAsO0.60F0.12 superconductor. J Appl Phys. 2013;113:183902. Available from: https://doi.org/10.1063/1.4803875

94. Kim MJ, Ratcliff W 2nd, Pajerowski DM, Kim JW, Yan JQ, et al. Magnetic ordering and structural distortion in a PrFeAsO single crystal studied by neutron and X-ray scattering. Phys Rev B. 2021;103:174405. Available from: https://doi.org/10.1103/PhysRevB.103.174405

95. Bernardini F, Garbarino G, Sulpice A, Núñez-Regueiro M, Gaudin E, Chevalier B, et al. Iron-based superconductivity extended to the novel silicide LaFeSiH. Phys Rev B. 2018;97:100504(R). Available from: https://doi.org/10.1103/PhysRevB.97.100504

96. Bhattacharyya A, Rodière P, Vaney J-B, Biswas PK, Hillier AD, Bosin A, et al. Evidence of nodal superconductivity in LaFeSiH. Phys Rev B. 2020;102:224502. Available from: https://doi.org/10.1103/PhysRevB.101.224502

97. Hansen MF, Layek S, Vaney J-B, Chaix L, Suchomel MR, Mikolasek M, et al. Magnetic and structural properties of the iron silicide superconductor LaFeSiH. Phys Rev B. 2024;109:174523. Available from: https://doi.org/10.1103/PhysRevB.109.174523

98. Hansen MF, Vaney JB, de Rango P, Salaun M, Tence S, et al. In-situ deuteration study of LaFeSi into superconducting LaFeSi(H,D). J Alloys Compd. 2023;169281. Available from: https://hal.science/hal-04029090v1/file/01122022_In_situ_hydrogenation_of_LaFeSi.pdf

99. Sourd J, Vignolle B, Gaudin E, Burdin S, Tence S. Superconductivity, Kondo physics and magnetic order: tuning the ground state in the La1-xCexFeSiH solid solution through the interplay between 3d and 4f correlated electrons. arXiv [Preprint]. 2026. arXiv:2601.04097. Available from: https://doi.org/10.1103/flxt-1x8g

100. Tapp JH, Tang Z, Lv B, Sasmal K, Lorenz B, Chu PCW, Guloy AM, et al. LiFeAs: an intrinsic FeAs-based superconductor with Tc = 18 K. Phys Rev B. 2008;78:060505(R). Available from: https://doi.org/10.1103/PhysRevB.78.060505

101. Chu CW, Chen F, Gooch M, Guloy AM, Lorenz B, Lv B, et al. The synthesis and characterization of LiFeAs and NaFeAs. Physica C. 2009;469:326-331. Available from: https://doi.org/10.48550/arXiv.0902.0806

102. Umezawa K, Li Y, Miao H, Nakayama K, Liu ZH, Richard P, et al. Unconventional anisotropic s-wave superconducting gaps of the LiFeAs iron-pnictide superconductor. Phys Rev Lett. 2012;108:037002. Available from: https://doi.org/10.1103/physrevlett.108.037002

103. Kim H, Tanatar MA, Song YJ, Kwon YS, Prozorov R. Nodeless two-gap superconducting state in single crystals of the stoichiometric iron pnictide LiFeAs. Phys Rev B. 2011;83:100502(R). Erratum in: Phys Rev B. 2011;83:109903. Available from: https://doi.org/10.1103/PhysRevB.83.100502

104. Day RP, Na MX, Zingl M, Zwartsenberg B, Michiardi M, Levy G, et al. The three-dimensional electronic structure of LiFeAs: strong-coupling superconductivity and topology in the iron pnictides. Phys Rev B. 2021;105:155142. Available from: https://doi.org/10.1103/PhysRevB.105.155142

105. Platt C, Thomale R, Hanke W. From density functional theory to the functional renormalization group: superconductivity in the iron pnictide LiFeAs. Phys Rev B. 2011;84:235121. Available from: https://doi.org/10.48550/arXiv.1103.2101

106. Brydon PMR, Daghofer M, Timm C, van den Brink J. Theory of magnetism and triplet superconductivity in LiFeAs. Phys Rev B. 2011;83:060501(R). Available from: https://doi.org/10.1103/PhysRevB.83.060501

107. Ma L, Zhang J, Chen GF, Yu W. NMR evidence of strongly correlated superconductivity in LiFeAs: tuning toward a spin-density-wave ordering. Phys Rev B. 2010;82:180501(R). Available from: https://doi.org/10.1103/PhysRevB.82.180501

108. Parker DR, Pitcher MJ, Baker PJ, Franke I, Lancaster T, Blundell SJ, Clarke SJ. Structure and superconductivity in NaFeAs. Chem Commun (Camb). 2009:2189-2191. Available from: https://doi.org/10.1039/b818911k

109. Chen GF, Hu WZ, Luo JL, Wang NL. Multiple phase transitions in single-crystalline Na1-δFeAs. Phys Rev Lett. 2009;102:227004. Available from: https://doi.org/10.1103/physrevlett.102.227004

110. Yi M, Lu DH, Moore RG, Kihou K, Lee CH, Iyo A, et al. Electronic reconstruction through the structural and magnetic transitions in detwinned NaFeAs. New J Phys. 2012;14:073019. Available from: https://arxiv.org/pdf/1111.6134

111. He C, Zhang Y, Wang XF, Jiang J, Chen F, Yang LX, et al. The orbital characters and kz dispersions of bands in iron-pnictide NaFeAs. J Phys Chem Solids. 2011;72(5):479-482. Available from: https://doi.org/10.1016/j.jpcs.2010.10.078

112. Watson MD, Aswartham S, Rhodes LC, Parrett B, Iwasawa H, Hoesch M, et al. Three-dimensional electronic structure of the nematic and antiferromagnetic phases of NaFeAs. Phys Rev B. 2018;97:035134. Available from: https://doi.org/10.1103/PhysRevB.97.035134

113. Rosenthal EP, Andrade EF, Arguello CJ, Fernandes RM, Xing LY, Wang XC, et al. Visualization of electron nematicity and unidirectional antiferroic fluctuations at high temperatures in NaFeAs. Nat Phys. 2014;10:225-232. Available from: https://doi.org/10.1038/nphys2870

114. Nekrasov IA, Pavlov NS, Sadovskii MV. Electronic structure of NaFeAs superconductor: LDA+DMFT calculations compared to the ARPES experiment. JETP Lett. 2015;102:26-31. Available from: https://doi.org/10.1134/S0021364015130123

115. Deng Z, Wang XC, Liu QW, Zhang SJ, Lv YX, Zhu JL, et al. A new "111" type iron pnictide superconductor LiFeP. Europhys Lett. 2009;87(3):37004.

116. Ferber J, Jeschke HO, Valentí R. Fermi surface topology of LaFePO and LiFeP. Phys Rev Lett. 2012;109:236403.

117. Kim JS, Xing LY, Wang XC, Jin CQ, Stewart GR. LiFeP: a nodal superconductor with an unusually large ΔC/Tc. Phys Rev B. 2013;87:054504. Available from: https://doi.org/10.1103/PhysRevB.87.054504

118. Zala VB, Vora AM, Gajjar PN. Electronic properties of iron pnictide superconductor LiFeP. AIP Conf Proc. 2019;2100:020027. Available from: https://www.semanticscholar.org/paper/Electronic-properties-of-iron-pnictide-LiFeP-Zala-Vora/42ab3b9cd276e94268734c8e04c2b4defcc4bfb5

119. Hsu FC, Luo JY, Yeh KW, Chen TY, Huang TW, Wu PM, et al. Superconductivity in the PbO-type structure α-FeSe. Proc Natl Acad Sci U S A. 2008;105:(38)14262-14264. Available from: https://doi.org/10.1073/pnas.0807325105

120. McQueen TM, Huang Q, Ksenofontov V, Felser C, Xu Q, Zandbergen H, et al. Extreme sensitivity of superconductivity to stoichiometry in Fe1+δSe. Phys Rev B. 2009;79:014522. Available from: https://doi.org/10.1103/PhysRevB.79.014522

121. Subedi A, Zhang L, Singh DJ, Du MH. Density functional study of FeS, FeSe, and FeTe: electronic structure, magnetism, phonons, and superconductivity. Phys Rev B. 2008;78:134514. Available from: https://doi.org/10.1103/PhysRevB.78.134514

122. Rotter M, Tegel M, Johrendt D. Superconductivity at 38 K in the iron arsenide (Ba1-xKx)Fe2As2. Phys Rev Lett. 2008;101(10):107006. Available from: https://doi.org/10.1103/PhysRevLett.101.107006

123. Sefat AS, Jin R, McGuire MA, Sales BC, Singh DJ, Mandrus D. Superconductivity at 22 K in Co-doped BaFe2As2 crystals. Phys Rev Lett. 2008;101:117004. Available from: https://doi.org/10.1103/PhysRevLett.101.117004

124. Sen S, Ghosh H. Fermiology of the 122 family of Fe-based superconductors: an ab initio study. Phys Lett A. 2015;379(9):843-847.

125. Tarantini C, Alam Limon S, Mao K, Hellstrom EE, Kametani F. Evidence of multiscale supercurrents in K-doped BaFe2As2. Supercond Sci Technol. 2025;38:045023. Available from: https://www.osti.gov/servlets/purl/3011585

126. Li LJ, Luo YK, Wang QB, Chen H, Ren Z, Tao Q, et al. Superconductivity induced by Ni doping in BaFe2As2 single crystals. New J Phys. 2009;11:025008. Available from: https://ui.adsabs.harvard.edu/link_gateway/2009NJPh...11b5008L/doi:10.48550/arXiv.0809.2009

127. Sun DL, Xiao JZ, Lin CT. Growth and annealing effect of Co-doped BaFe2As2 single crystals. J Cryst Growth. 2011;323(1):55-59. Available from: https://doi.org/10.1016/j.jcrysgro.2011.02.033

128. Sasmal K, Lv B, Lorenz B, Guloy AM, Chen F, Xue YY, Chu CW. Superconducting Fe-based compounds (A1-xSrx)Fe2As2 with A = K and Cs with transition temperatures up to 37 K. Phys Rev Lett. 2008;101(10):107007. Available from: https://doi.org/10.1103/physrevlett.101.107007

129. Marra P, Nigro A, Li Z, Chen GF, Wang NL, Luo JL, Noce C. Paraconductivity of the K-doped SrFe2As2 superconductor. New J Phys. 2012;14:043001. Available from: https://doi.org/10.1088/1367-2630/14/4/043001

130. Leithe-Jasper A, Schnelle W, Geibel C, Rosner H. Superconducting state in SrFe2-xCoxAs2 by internal doping of the iron-arsenide layers. Phys Rev Lett. 2008;101:207004. Available from: https://doi.org/10.1103/PhysRevLett.101.207004

131. Lv B, Deng L, Gooch M, Wei F, Sun Y, et al. Unusual superconducting state at 49 K in electron-doped CaFe2As2 at ambient pressure. Proc Natl Acad Sci U S A. 2011;108(38):15705-15709. Available from: https://doi.org/10.1073/pnas.1112150108

132. Shirage PM, Kihou K, Lee CH, Kito H, Eisaki H, Iyo A. Superconductivity at 28.3 and 17.1 K in (Ca4Al2O6-y)(Fe2Pn2) (Pn = As, P). Appl Phys Lett. 2010;97:172506. Available from: https://doi.org/10.1063/1.3508957

133. Shirage PM, Kihou K, Lee CH, Kito H, Eisaki H, Iyo A. Discovery of the Ca4Al2O6Fe2Pn2 "Al-42622(Pn)" and Ca3Al2O5Fe2Pn2 "Al-32522(Pn)" (Pn = As, P) superconductors. Physica C. 2013;484:12-15.